its volume ($\propto r^3$) grows linearly with time because of the steady supply of Si from the vapor phase. Equation 2 predicts that if we plot r^3/R^3 versus $(P/R)(t - t_n)$ for all the measurements at a given temperature, the data should collapse onto a single curve. This is confirmed in Fig. 2D for data obtained from different experiments at a fixed temperature of 525°C and covering a wide range of disilane pressures and droplet sizes. All the data sets show essentially the same jump (that is, the same supersaturation) and the same slope. This is an important test of the model and the assumptions underlying Eqs. 1 and 2. In particular, the collapse of the data onto a single curve confirms that there is no strong dependence of any of the model parameters, such as the shape factors, rate constants, and supersaturation, on P or on R, the system size.

Size effects in nucleation have been studied for decades. Until recently, the only observed size effects were attributed to defects or impurities (*1*, *3*, *21*), although the possibility of intrinsic size effects due to the number of available sites was also considered (*21*). The extrinsic size effects disappeared when the system was so small that it contained no impurities (*1*, *3*, *21*). More recently, there have been reports of dramatic intrinsic size effects, with substantial changes in the fundamental phase diagram even for systems as large as 60 nm in diameter (*5*, *22*–*24*). It therefore was surprising to find no effect in our own data, with diameters between 12 and 40 nm.

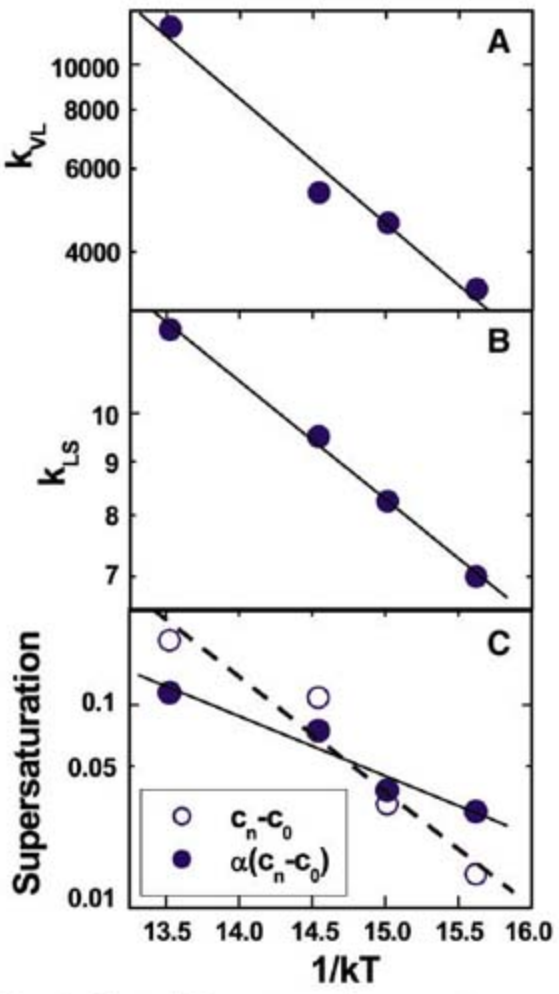

Fig. 3. (**A** to **C**) Parameter values versus temperature, shown on Arrhenius plots. These values are determined by fitting the entire data set shown in fig. S1, E to H. The solid and dashed lines are linear least-squares fits. (**A**) Vapor-liquid rate constant k_{VL}. (**B**) Liquid-solid rate constant k_{LS}. (**C**) Supersaturation at nucleation; solid circles indicate the parameter $\alpha(c_n - c_0)$ obtained directly from the fitting of Eq. 1 and open circles indicate the absolute supersaturation $c_n - c_0$ based on extrapolation from the growth kinetics after the jump. The two analyses exhibit a similar trend, in that the supersaturation at nucleation increases strongly with temperature.

Thermodynamics predicts that the liquidus concentration c_0 shifts by an amount roughly proportional to γ/R, whereas size effects on c_n are expected to be negligibly small by comparison (*17*). Here, γ involves geometrically weighted differences of the respective interfacial energies in the system, so it is highly system-dependent and has not to our knowledge been determined for any VLS system. Thus, we could not predict the magnitude of size effect expected, so we focused on the size scaling. For each temperature, our data span roughly a factor of 2 in size, so whatever size effects occur at our smallest size should be reduced by half at our largest size. Figure 2D shows that the scatter in jump height is very small; more quantitatively, we estimate that changes in $\alpha(c_n - c_0)$ due to size are not more than 0.005 (0.5%), otherwise they would be observable as a systematic trend above the scatter. We therefore found a lack of sensitivity to size over the important range used to form nanowires for device applications, which is helpful for predictably engineering small structures.

Furthermore, we found that nucleation systematically occurs at the droplet edge, indicating that it is heterogeneous, with both surface and interface playing a role. This implies that the supersaturation needed for nucleation, and possibly even the extent of size effects, could be rather different on another substrate and could be altered by appropriate pretreatment of the substrate. Yet the nucleation is intrinsic, being highly reproducible from drop to drop. Both facts are favorable for technological applications; reproducibility is essential for large-scale integration, and the role of the substrate in nucleation suggests opportunities for control via substrate engineering.

We now discuss the numerical values and physical importance of the fitted parameters. If we knew the three-dimensional shapes, and hence the geometric factors, the results in Fig. 3 would correspond to direct measurements of the two rate constants k_{VL} and k_{LS} and the critical supersaturation $c_n - c_0$. Even without this knowledge, we can determine the temperature dependences of the physical parameters if we assume that the shapes are independent of temperature. The kinetic rate constants are expected to be thermally activated, and indeed the measured values are consistent with this (Fig. 3). The slope for k_{VL} gives an activation energy of about 0.61 eV for the dissociative adsorption of disilane, in agreement with previous work (*19*). The slope for k_{LS} gives an activation energy of about 0.26 eV for incorporation of Si from the AuSi liquid into the Si crystal. And the parameter $\alpha(c_n - c_0)$ ranges from 3 to 12%, increasing with temperature.

The unknown geometrical factors are expected to be of order 1. But their presence causes uncertainty in extracting supersaturation from the parameter $\alpha(c_n - c_0)$. However, we can estimate the supersaturation without knowledge of the geometrical factors by using an entirely different approach (*17*). It relies on the assumption that the rate of addition of Si to the droplet is approximately constant over time and can be determined from the time to reach c_0 (the x intercept of the dotted line in Fig. 2D). In Fig. 3C, we show values of supersaturation calculated using this approach. The results are similar to the results from the direct fitting, and the ratio (which ideally should be α) is of order 1, as expected for reasonable geometries. Both data sets in Fig. 3C show a similar trend with temperature. There is a difference in the slope, which could arise if the α values depend on temperature (such as via the drop contact angle) or if there are other systematic deviations from our simplifying assumptions. In any case, two quite different approaches lead to the same conclusion, namely that the supersaturation at nucleation increases strongly with temperature.

The temperature dependence of the supersaturation is intriguing. We are not aware of prior results that explain this, and we can only speculate about the mechanism. The required supersaturation is controlled largely by the interfacial free energy of the Si nucleus (*2*), so the temperature dependence of $c_n - c_0$ is likely to track the temperature dependence of this energy. The results are consistent with an Arrhenius behavior, with the smaller values at low temperature suggesting a reduced interface energy at low temperature. Temperature-dependent interface energies may be related to a temperature-dependent near-surface ordering that has recently been observed in AuSi (*25*) or to hydrogen coverage at the Si-vapor interface, which could depend on T via thermally activated disilane-cracking and H desorption.

We have shown detailed measurements of a nucleation and growth phenomenon, exploring the phase diagram of a nanoscale system at constant temperature and varying composition. The growth kinetics are explained by the buildup of a substantial supersaturation before nucleation. The lack of any change in supersaturation with system size suggests that the phase diagram has no appreciable size dependence in this system, at least down to ~12 nm in diameter.

We believe that the results shown here are of fundamental interest in advancing the theoretical understanding of nucleation in nanoscale systems, a phenomenon that is of importance in materials design for nanotechnology and in crystal growth and phase transformations. The results are particularly relevant to the growth of nano-

wires from liquid eutectic droplets, the most common route of nanowire formation. A detailed understanding of nucleation and growth kinetics will help in engineering nanostructures for applications such as sensors, transistors, and logic circuits (*26*), in which size dependence, incubation times, and the reliability of nucleation itself must all be controlled for the successful fabrication of each nanoscale device.

References and Notes

1. D. Turnbull, R. E. Cech, *J. Appl. Phys.* **21**, 804 (1950).
2. D. Turnbull, J. C. Fisher, *J. Chem. Phys.* **17**, 71 (1949).
3. J. H. Perepezko, J. L. Sebright, P. G. Höckel, G. Wilde, *Mater. Sci. Eng. A* **326**, 144 (2002).
4. Y. Wu, P. Yang, *J. Am. Chem. Soc.* **123**, 3165 (2001).
5. P. W. Sutter, E. A. Sutter, *Nat. Mater.* **6**, 363 (2007).
6. B. Kalache, P. R. I. Cabarrocos, A. Fontcuberta i Moral, *Jpn. J. Appl. Phys.* **45**, L190 (2006).
7. T. Clement, S. Ingole, S. Ketharanathan, J. Drucker, S. T. Picraux, *Appl. Phys. Lett.* **89**, 163125 (2006).
8. K. C. Lu *et al.*, *Nano Lett.* **7**, 2389 (2007).
9. S. K. Eswaramoorthy, J. M. Howe, G. Muralidharan, *Science* **318**, 1437 (2007).
10. S. Hofmann *et al.*, *Nat. Mater.* **7**, 372 (2008).
11. R. S. Wagner, W. C. Ellis, *Appl. Phys. Lett.* **4**, 89 (1964).
12. C. Thelander *et al.*, *Mater. Today* **9**, 28 (2006).
13. V. Schmidt *et al.*, *Small* **2**, 85 (2006).
14. O. Hayden *et al.*, *Small* **3**, 230 (2007).
15. M. Hammar, F. K. LeGoues, J. Tersoff, M. C. Reuter, R. M. Tromp, *Surf. Sci.* **349**, 129 (1996).
16. F. M. Ross, J. Tersoff, M. C. Reuter, *Phys. Rev. Lett.* **95**, 146104 (2005).
17. Materials and methods are available as supporting material on *Science* Online.
18. R. P. Sear, *J. Phys. Condens. Matter* **19**, 033101 (2007).
19. S. Kodambaka, J. Tersoff, M. C. Reuter, F. M. Ross, *Phys. Rev. Lett.* **96**, 096105 (2006).
20. To establish this, we measured Au crystallite sizes and AuSi droplet sizes during annealing without growth. We did not observe appreciable changes in size, even for the smallest particles, which shows that Ostwald ripening need not be considered in these experiments.
21. T. Takahashi, W. A. Tiller, *Acta Metall.* **17**, 643 (1969).
22. J. G. Lee, H. Mori, *Phys. Rev. Lett.* **93**, 235501 (2004).
23. E. Sutter, P. Sutter, *Nano Lett.* **8**, 411 (2008).
24. H. Adhikari, A. F. Marshall, C. E. D. Chidsey, P. C. McIntyre, *Nano Lett.* **6**, 318 (2006).
25. O. G. Shpyrko *et al.*, *Science* **313**, 77 (2006).
26. W. Lu, C. M. Lieber, *J. Phys. D Appl. Phys.* **39**, R387 (2006).

27. We acknowledge A. Ellis and K. B. Reuter of IBM for their assistance with experimental aspects of this work, M. Comer of Purdue with assistance in image analysis, and financial assistance from NSF under grant DMR-0606395.

Supporting Online Material

www.sciencemag.org/cgi/content/full/322/5904/1070/DC1
Materials and Methods
Figs. S1 and S2
Movie S1 and S2

21 July 2008; accepted 17 October 2008
10.1126/science.1163494

Spectroscopic Tracking of Structural Evolution in Ultrafast Stilbene Photoisomerization

Satoshi Takeuchi,[1] Sanford Ruhman,[2] Takao Tsuneda,[3] Mahito Chiba,[4] Tetsuya Taketsugu,[5] Tahei Tahara[1]*

Understanding a chemical reaction ultimately requires the knowledge of how each atom in the reactants moves during product formation. Such knowledge is seldom complete and is often limited to an oversimplified reaction coordinate that neglects global motions across the molecular framework. To overcome this limit, we recorded transient impulsive Raman spectra during ultrafast photoisomerization of *cis*-stilbene in solution. The results demonstrate a gradual frequency shift of a low-frequency spectator vibration, reflecting changes in the restoring force along this coordinate throughout the isomerization. A high-level quantum-chemical calculation reproduces this feature and associates it with a continuous structural change leading to the twisted configuration. This combined spectroscopic and computational approach should be amenable to detailed reaction visualization in other photoisomerizing systems as well.

Molecular rearrangements in chemical reactions occur on a time scale comparable to nuclear vibrational periods (i.e., from 10 fs to 1 ps). This time scale is now accessible with advanced ultrafast vibrational spectroscopy (*1*), but, in almost all studies, we only observe structures in stationary (excited) states and the population transfer from one state to the other. Continuous changes of the molecular structure are seldom observed, especially for large polyatomic molecules. This situation often limits our understanding to a level of an oversimplified reaction coordinate (RC). To map structural evolution and elucidate true RCs, it is crucial to track molecular vibrations during reactions, which characterize the global motions of the whole molecule. Recently, femtosecond infrared spectroscopy has provided highly time-resolved vibrational spectra, but the technique is practically limited to the >1000 cm^{-1} region (*2*). Conventional spontaneous Raman is only applicable to picosecond or slower processes, because long and narrow-band pulses are utilized to achieve sufficient frequency resolution (<15 cm^{-1}). This drawback in time resolution was improved by the introduction of a stimulated Raman process with femtosecond pulses (*3*). With the use of this technique, geometric changes of the retinyl chromophore in visual pigments were uncovered by monitoring hydrogen out-of-plane wagging vibrations in the 800- to 1000-cm^{-1} region (*4*). Common to these frequency-domain Raman approaches, however, is the challenge of observing low-frequency vibrations, given disturbance from strong Rayleigh scattering. Here we report a femtosecond resonance Raman probing at the impulsive limit to follow the low-frequency spectral change accompanying structural evolution in a cis-trans photoisomerization in solution.

Femtosecond transient impulsive Raman spectroscopy is explained as a combined pump-probe and time-domain Raman technique using three laser pulses (*5*, *6*), as shown in Fig. 1A (*7*). In this experiment, we first generate a reactive excited-state molecule by a pump pulse (P_1). After a certain delay (ΔT), we introduce an ultrashort pulse (P_2) resonant with the excited-state absorption and impulsively induce a vibrational coherence of Raman active modes, which is driven by two frequency components contained in the spectrum of the P_2 pulse. In other words, the P_2 pulse initiates the motion of a nuclear wave packet in the reactive excited state. The third pulse (P_3) monitors the excited-state absorption, whose intensity is modulated by the nuclear wave-packet motion. Fourier transformation of the resultant beating feature in the time-resolved absorption provides a spectrum of the molecular vibration with a detectable range reaching into the low-frequency terahertz region, which is inaccessible by other frequency-domain methods. For long-lived stationary states, this time-domain measurement gives vibrational information equivalent to that obtainable from conventional frequency-domain Raman (*8*, *9*). However, for structurally evolving states in a picosecond, this method can afford vibrational spectra with the best possible time- and frequency-resolutions that are determined only by the vibrational coherence time of the transients.

Stilbene is an extensively studied paradigm of ultrafast olefinic photoisomerization (Fig. 1B). In particular, *cis*-stilbene exhibits nearly barrierless bond twisting in the excited state that is complete within ~1 ps (*10*–*15*). The photoisomerization mechanism of *cis*-stilbene has been often discussed on the basis of a traditional one-dimensional (1D) potential energy surface (PES) along the torsional coordinate of the cen-

[1]Molecular Spectroscopy Laboratory, RIKEN, 2-1 Hirosawa, Wako 351-0198, Japan. [2]Institute of Chemistry, Hebrew University, Jerusalem 91904, Israel. [3]School of Engineering, University of Tokyo, Tokyo 113-8656, Japan. [4]National Institute of Advanced Industrial Science and Technology, Tsukuba 305-6568, Japan. [5]Graduate School of Science, Hokkaido University, Sapporo 060-0810, Japan.

*To whom correspondence should be addressed. E-mail: tahei@riken.jp

tral C=C bond in the first singlet electronic excited (S_1) state (Fig. 1A) (*16*). The S_1 PES is believed to have a rather flat feature on the cis side, where the excited molecule persists for ~1 ps as an isomerization precursor showing strong $S_n \leftarrow S_1$ absorption in the 600- to 700-nm region (here, S_n is a higher-lying electronic excited state). Then, the molecule migrates to an S_1/S_0 conical intersection and relaxes to either the trans (product) or cis isomer in the ground (S_0) state. However, spectroscopic studies have pointed to the inadequacy of this 1D rigid-twist model that does not take into account, for example, out-of-plane deformations of the ethylenic moiety (*17*, *18*). Pyramidalization of one ethylenic carbon ($sp^2 \rightarrow sp^3$ change of hybridization) was recently claimed to be essential in the structure at the S_1/S_0 conical intersection, indicating the importance of the multidimensionality of PES (*19*). For elucidation of the true RC of the polyatomic molecule, it is crucial to track the structural evolution by taking a temporal series of spectroscopic snapshots of the molecule.

To achieve this aim, we acquired femtosecond impulsive Raman data of *cis*-stilbene over the course of the isomerization. Figure 1C presents a time-resolved $S_n \leftarrow S_1$ absorption in the absence of the P_2 pulse after excitation with the 267-nm P_1 pulse. This signal shows a 1.3-ps decay, reflecting a decrease in the S_1 population due to internal conversion/isomerization (*11*–*13*, *15*). With irradiation by the P_2 pulse (11 fs, 620 nm) after a delay ΔT, the $S_n \leftarrow S_1$ absorption instantaneously changes, because the P_2 pulse resonantly excites a fraction of the S_1 molecules to the S_n state. The difference between the $S_n \leftarrow S_1$ absorption signals measured with and without the P_2 pulse gives time-resolved impulsive Raman data, which include information about the nuclear wave-packet motion induced by the P_2 pulse. With the P_2 pulse tuned in rigorous resonance with absorption of the isomerization precursor, this impulsive Raman measurement selectively monitors the photoisomerization process, and the signal contribution from a minor photocyclization to 4a,4b-dihydrophenanthrene is negligible (*20*). We measured time-resolved impulsive Raman signals in hexadecane at three delays (ΔT = 0.3, 1.2, and 2 ps) to examine the temporal change of S_1 vibrational structure (Fig. 2A). A strong beating feature is observed in each trace, which reflects the nuclear wave-packet motion induced in S_1 *cis*-stilbene at each delay. A contribution from the S_n state is excluded because its lifetime is shorter than the damping time of the beating. The other features of the observed traces are represented by three exponential decay components that reflect the population dynamics after the P_1 and P_2 irradiation (*21*).

The inset of Fig. 2A shows the beating features extracted from the data by subtraction of the population component. Their Fourier transform power spectra (Fig. 2B) represent vibrational spectra of S_1 *cis*-stilbene at the three ΔT delays. At ΔT = 0.3 ps, a broad band appears near 240 cm^{-1}, together with several weak bands at 411, 533, and 752 cm^{-1}. As the only band showing exceptionally large Raman intensity in the 200- to 300-cm^{-1} region, the predominant 240-cm^{-1} band is characteristic of S_1 *cis*-stilbene; hence, it is straightforwardly associated with a broad band observed near 229 cm^{-1} in a picosecond frequency-domain Raman study (*22*). This vibration has been assigned to a mode that involves the motion of phenyl-C=C bending, ethylenic C=C torsion, and phenyl torsion. The nuclear wave-packet motion due to the same mode was also observed in previous ultrafast uv-pump/vis-probe measurements in this laboratory (*23*), which detected the nuclear wave-packet motion induced directly by photoexcitation.

The present Raman measurements reveal that the center frequency of the 240-cm^{-1} motion considerably downshifts with increasing ΔT delay, diminishing from 239 cm^{-1} (ΔT = 0.3 ps) to 224 cm^{-1} (1.2 ps) to 215 cm^{-1} (2 ps). This large frequency downshift is directly apparent in the raw time-domain data. As shown in the inset of Fig. 2A, the intensity maxima of the three beating components gradually shift in time, manifesting a lengthening of the oscillation period with increasing delay. The data reveal that the frequency of the 240-cm^{-1} mode substantially changes while the isomerization proceeds. In other words, the 240-cm^{-1} mode probes the structural evolution of the molecule as a spectator through a large anharmonic coupling to the isomerization coordinate.

To confirm that the frequency downshift is directly related to the isomerization process, we carried out the same measurements in methanol, where the isomerization is accelerated and proceeds with a time constant of 0.48 ps (*13*, *15*). The data obtained at ΔT = 0.3, 0.7, and 1.1 ps (Fig. 2, B and C) show that the 240-cm^{-1} mode exhibits a clear frequency downshift in methanol also. Figure 2D compares the temporal change of the center frequency of the mode in the two solvents. Clearly, the rate of the frequency downshift is higher in methanol than in hexadecane. With the change of solvent from hexadecane to methanol, the isomerization rate increases by a factor of 2.7 (0.77 to 2.08 ps^{-1}), and the rate of the frequency downshift nearly doubles (14 versus 27 cm^{-1}/ps). This strong correlation confirms that the frequency downshift of the 240-cm^{-1} mode arises from the structural evolution relevant to the isomerization of S_1 *cis*-stilbene.

Linear fits to the frequency shifts observed in the two solvents both extrapolate to the same initial frequency (242 ± 2 cm^{-1}) at zero delay (*24*). We independently evaluated the initial frequency of this mode in a uv-pump/vis-probe experiment (*23*) (where the nuclear wave-packet motion was directly induced by $S_1 \leftarrow S_0$ photo-

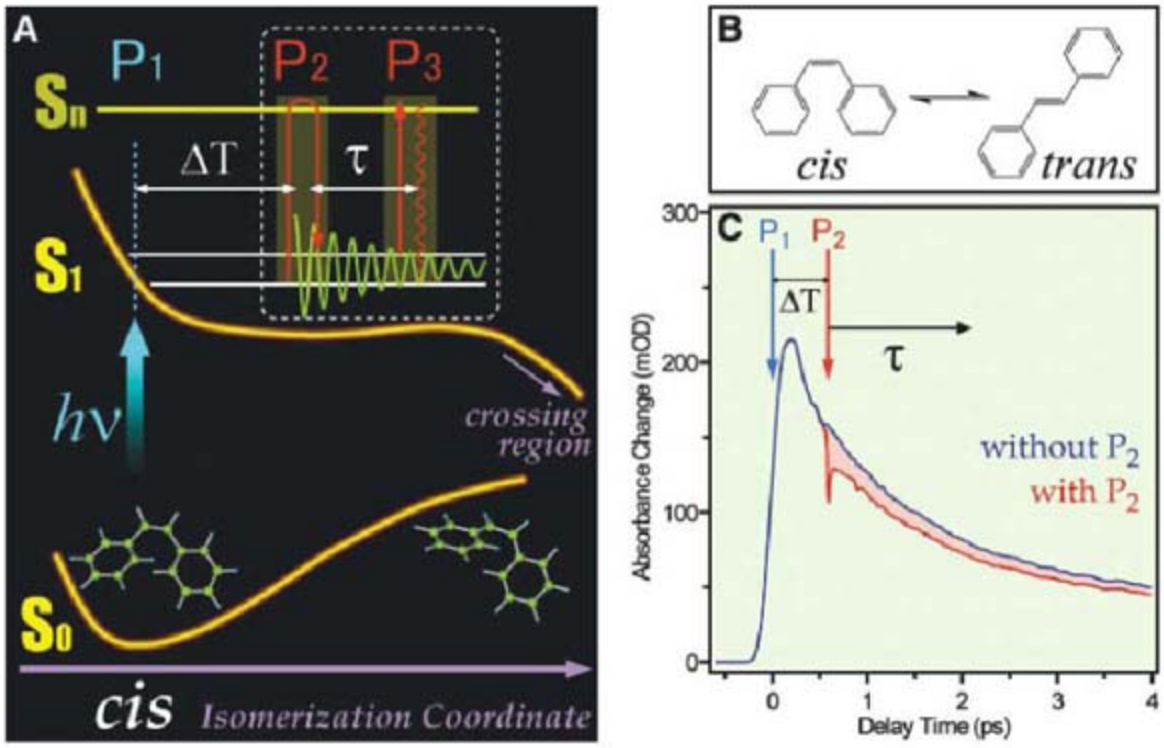

Fig. 1. (**A**) Schematic illustration of the S_0, S_1, and S_n PESs of *cis*-stilbene against the isomerization coordinate, together with a sequence of three laser pulses used in the measurements. The first pulse (P_1; 267 nm, 150 fs) photoexcites S_0 *cis*-stilbene in solution and generates the reactive S_1 state. It does not efficiently generate vibrational coherences in the S_1 molecule because of its relatively long duration. After a delay ΔT, the second ultrashort pulse (P_2; 620 nm, 11 fs), which is resonant with the $S_n \leftarrow S_1$ transient absorption, is applied to generate a nuclear wave packet in the S_1 state. The third pulse (P_3; 620 nm, 11 fs) is used to monitor time-resolved $S_n \leftarrow S_1$ absorption signals. h, Planck's constant; ν, frequency; τ, delay time for impulsive Raman measurements. (**B**) Photoisomerization reaction of stilbene between the cis and trans isomers. (**C**) Typical time-resolved traces of the $S_n \leftarrow S_1$ absorption of *cis*-stilbene measured with and without the P_2 pulse. The difference between the two traces, shaded in red, gives a time-resolved impulsive Raman signal, which contains information about the S_1 wave-packet motion induced by the P_2 pulse. mOD, milli-optical density.

excitation) and found it to be 231 ± 3 cm^{-1} in both nonpolar (cyclohexane) and polar (methanol) solvents (*25*), which is 11 cm^{-1} lower than the value obtained from the extrapolation of the frequency shift after $\Delta T = 0.3$ ps. This discrepancy indicates that the frequency of this mode first exhibits an upshift as the wave packet evolves on the S_1 surface. In fact, we observed a shortening of the oscillation period in the uv-pump/vis-probe experiment (*23*), which demonstrates that the frequency upshift occurs within the vibrational coherence time. After this initial upshift, the mode shows a frequency downshift as observed in the present impulsive Raman experiment.

The vibrational period of the 240-cm^{-1} mode is approximately equal to 140 fs, which is well separated from the time scale of the isomerization (1.3 ps in hexadecane). Thus, the nuclear motion along the 240-cm^{-1} coordinate (q) can adjust adiabatically during the relatively slow temporal evolution of nuclear configurations due to the isomerization, with the instantaneous frequency of the 240-cm^{-1} mode decreasing as the isomerization proceeds. In other words, the vibrational force constant of the 240-cm^{-1} mode (k) decreases as the isomerization coordinate (Q) changes through the following anharmonic coupling relation (where V is potential energy)

$$\frac{\partial k}{\partial Q} = \frac{\partial}{\partial Q}\left(\frac{\partial^2 V}{\partial q^2}\right) = \frac{\partial^3 V}{\partial q^2 \partial Q} \neq 0 \qquad (1)$$

Because the force constant is given by the curvature of the S_1 PES along the 240-cm^{-1} coordinate (q), the present results reveal that the shape of the S_1 PES changes along the isomerization coordinate (*26*), as illustrated in Fig. 3B. The experiment shows that the structure of S_1 *cis*-stilbene continuously evolves within the S_1 lifetime. It is noteworthy that the "averaged" frequency measured in a picosecond frequency-domain Raman study (229 cm^{-1}) (*22*) lies in the middle of the range of the frequency shift (239 → 215 cm^{-1}) observed here.

To associate the experimental observation with actual structural changes in S_1 *cis*-stilbene, we calculated the PES and vibrational structure by density functional theory (DFT) and time-dependent DFT (TDDFT) using the Becke 1988 exchange + one-parameter progressive correlation functionals with long-range correction (*27*). The calculation gave a nonplanar optimized structure (C_2 symmetry) for S_0 *cis*-stilbene because of steric hindrances: The two phenyl groups are largely tilted ($\phi_{\beta\alpha 12} \approx 40°$), although the ethylene moiety is nearly planar ($\theta_{1\alpha\alpha' 1'} \approx 5°$). At this S_0 geometry, an optically allowed transition to the S_1 state, with a highest occupied molecular orbital → lowest unoccupied molecular orbital single-excitation character, was calculated at 4.90 eV, which agrees well with the experimental value (4.48 eV). Two almost-dark states were computed to lie above this bright S_1 state. The S_1 character, as well as the state ordering, is consistent with a recent calculation (*28*).

Starting from the S_1 state with the structure optimized for the S_0 state (Franck-Condon point), we gradually changed the geometry along the negative direction of mass-weighted energy gradients calculated at every point and searched the minimum energy path on the S_1 PES. The RC, s, is defined as the path length along the thus-obtained minimum energy path ($s = 0$ at the initial Franck-Condon point). Figure 4A depicts the change of the S_0 and S_1 energies along the RC. The S_1 energy first decreased rapidly ($s <$ 0.5) and then exhibited a slower decrease ($s >$ 0.5). This energy change reflects the biphasic structural evolution of the S_1 state. As shown in Fig. 4C, the initial structural change (Q_{init}) in $s <$ 0.5 is dominated by a prompt stretch of the central C=C bond due to $\pi\pi^*$ electronic excitation and an out-of-plane motion of the two ethylenic hydrogens. In the later region of $s > 0.5$, the two ethylenic hydrogens gradually move in opposite directions to a greater extent so that the

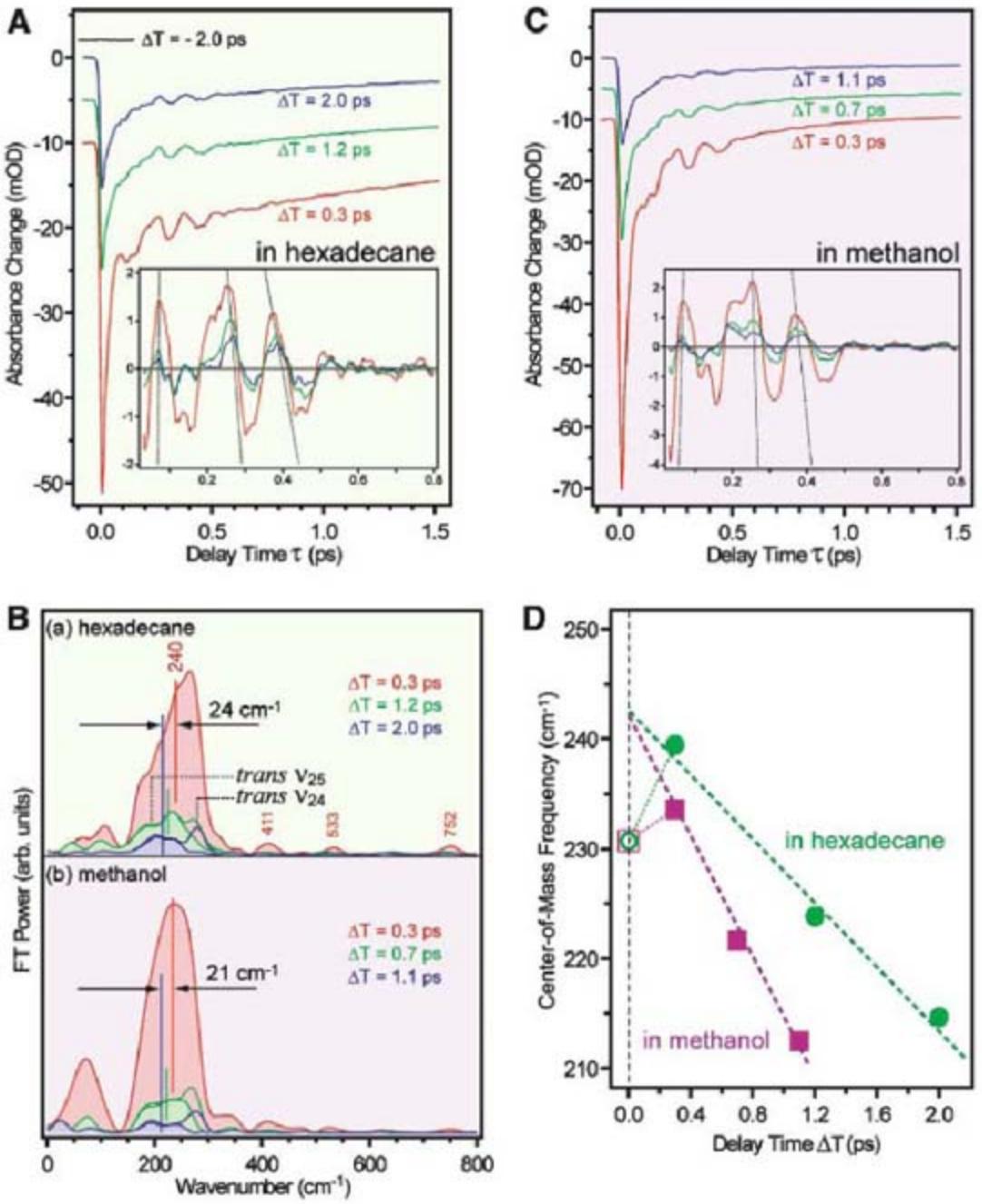

Fig. 2. Experimental results of the time-resolved impulsive Raman spectroscopy of *cis*-stilbene in two solvents. (**A** and **C**) Time-resolved impulsive Raman signals measured at three different ΔT delays in hexadecane and methanol, respectively. The measurements were carried out at room temperature with 0.02 mol dm^{-3} stilbene concentrations. The insets show the beating components obtained after subtraction of the population components. The dotted lines connect the corresponding maxima of the three beating components, and their tilt with time indicates that the oscillation period becomes longer with increasing ΔT delay. (**B**) Fourier transform (FT) power spectra of the beating components obtained at the three ΔT delays in (a) hexadecane and (b) methanol. Pure spectra of S_1 *cis*-stilbene (represented as the bands shaded in red, green, and blue for the three delays) were obtained after subtraction of weak bands due to the ν_{24} and ν_{25} modes of S_1 *trans*-stilbene (*30*) from the raw Fourier transform spectra represented by solid curves. The center-of-mass frequency of each *cis*-stilbene spectrum is indicated by a vertical line, which clearly shows a frequency downshift with time. (**D**) Plots of the center-of-mass frequency against ΔT delay for the two solvents. The rate of the frequency downshift after $\Delta T = 0.3$ ps, evaluated from the slope of this plot, is 14 cm^{-1}/ps in hexadecane and 27 cm^{-1}/ps in methanol.

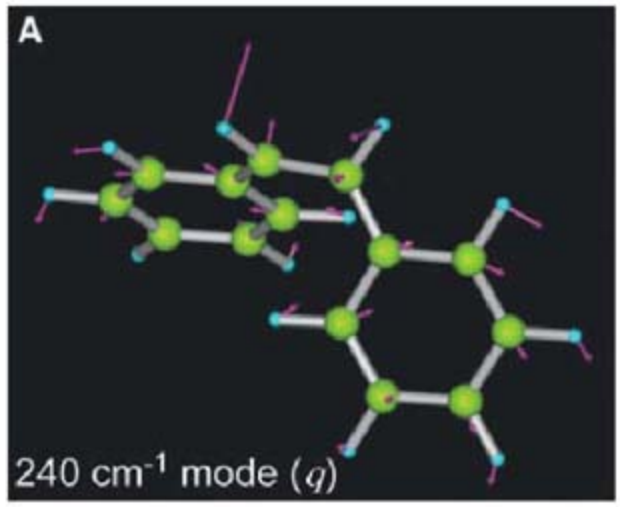

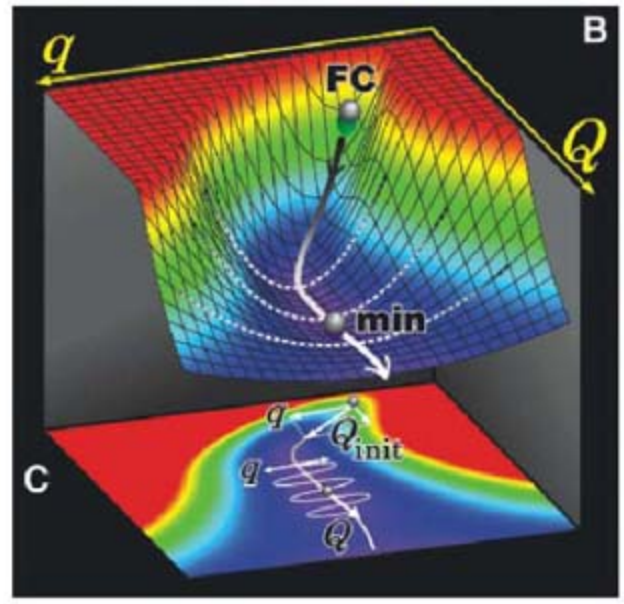

Fig. 3. **(A)** Nuclear motions of the 240-cm^{-1} mode at the geometry near the energy minimum on the S_1 PES (s = 5). **(B)** Schematic illustration of the S_1 PES of *cis*-stilbene against the isomerization coordinate (Q) and 240-cm^{-1} coordinate (ν_{33} mode, q) together with **(C)** the corresponding contour plot, which are drawn on the basis of the understanding obtained in the present study. The *cis*-stilbene molecule excited at the Franck-Condon point (FC) first shows a rapid structural change along a steep route (Q_{init}) that mainly involves a stretching of the central C=C bond with out-of-plane motion of the two ethylenic hydrogens. Then, a slower structural evolution toward the minimum point of the S_1 PES (min) ensues along the Q coordinate, which almost solely involves out-of-plane motion of the two ethylenic hydrogens (see text). The potential curvature along the q coordinate (indicated by dotted curves) becomes smaller as the molecule evolves along the isomerization coordinate.

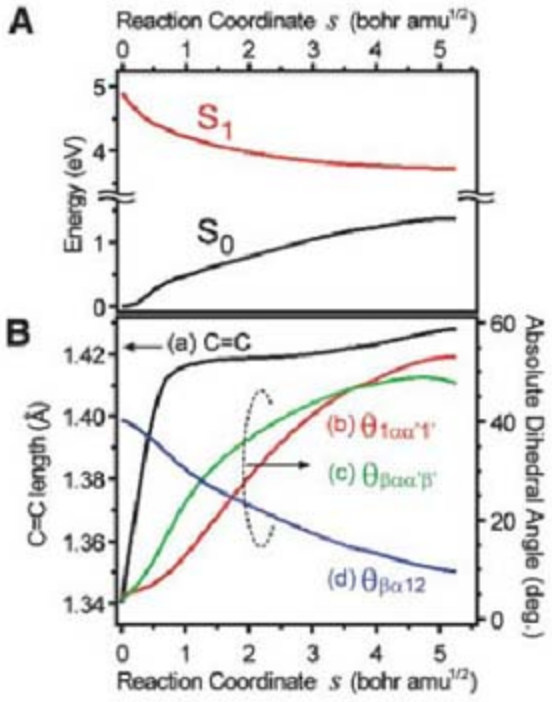

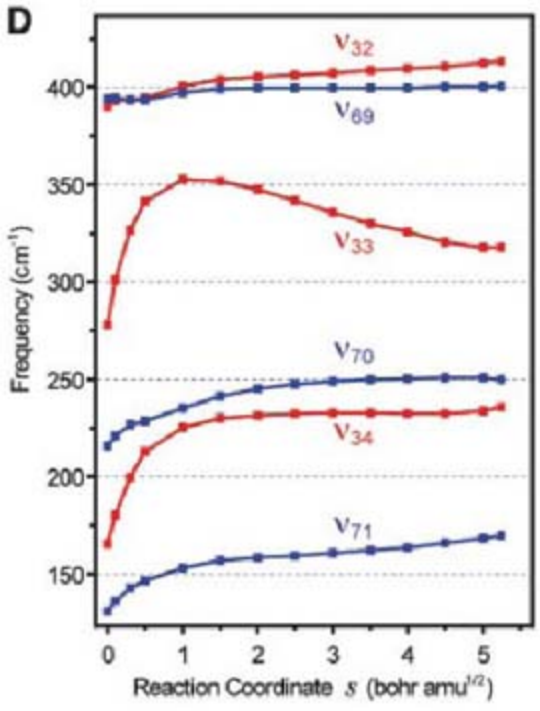

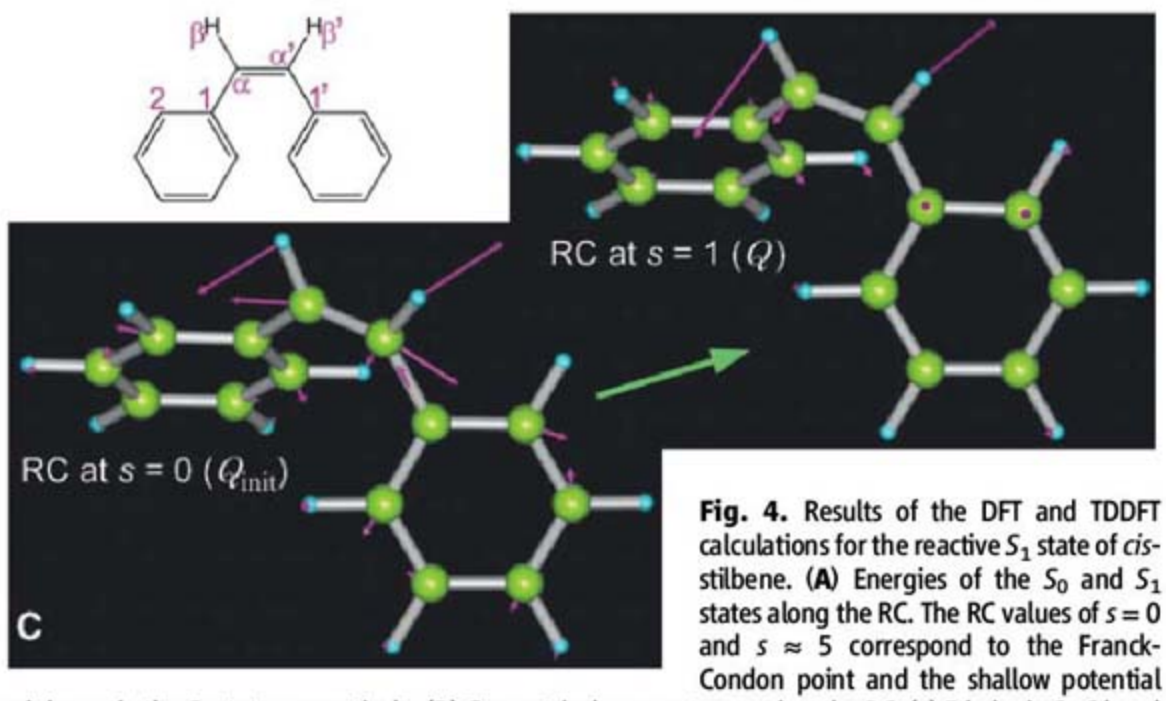

Fig. 4. Results of the DFT and TDDFT calculations for the reactive S_1 state of *cis*-stilbene. **(A)** Energies of the S_0 and S_1 states along the RC. The RC values of s = 0 and $s \approx 5$ correspond to the Franck-Condon point and the shallow potential minimum in the S_1 state, respectively. **(B)** Geometrical parameters against the RC. (a) Ethylenic C=C bond length; (b to d) dihedral angles. The atomic labeling is indicated below the figure. **(C)** RC vectors at s = 0 and s = 1, corresponding to Q_{init} and Q, respectively. **(D)** Calculated frequencies of several low-frequency modes of S_1 *cis*-stilbene against the RC. All the frequencies were scaled by a factor of 0.97. Vibrational modes with A and B symmetries are shown in red and blue, respectively.

twisting angle ($\theta_{\beta\alpha\alpha'\beta'}$) of the C=C bond increases and the tilt angle ($\phi_{\beta\alpha12}$) of the phenyl group decreases (*17*, *18*) (Fig. 4B). Consequently, a twisted structure having $\theta_{\beta\alpha\alpha'\beta'} \approx 49°$ and $\phi_{\beta\alpha12} \approx 10°$ is attained at $s \approx 5$, which corresponds to a very shallow potential minimum leading to the conical intersection. The substantial twisting around the C=C bond is achieved mainly by the out-of-plane motion of the ethylenic hydrogens without extensive motion of the phenyl rings. This twisting motion in the second phase, which actually characterizes the isomerization, cannot be fully detected by the analysis of resonance Raman spectra of the S_0 state (*17*), because it only sees the nuclear motions occurring within a very short electronic coherence time of the $S_1 \leftarrow S_0$ transition (a few tens of femtoseconds).

To calculate the instantaneous vibrational frequency during the structural evolution of S_1 *cis*-stilbene, we evaluated the force-constant matrix at different points along the RC and obtained the frequencies of the instantaneous normal modes. The calculated frequencies of six low-frequency modes are plotted against RC in Fig. 4D. Among these modes, the ν_{33} mode is uniquely assignable to the 240-cm^{-1} vibration observed in the experiment, on the basis of the frequency and Raman activity of this mode (*29*). The initial nuclear motion in $s < 0.5$ (Q_{init}) involves a substantial component parallel to the ν_{33} coordinate (q), and this motion is smoothly connected to the ν_{33} mode in the second phase ($s > 0.5$) (Fig. 3C). After a steep increase from 278 to 353 cm^{-1}, the ν_{33} frequency substantially decreases down to 318 cm^{-1} at the twisted geometry at s = 5. This behavior of the ν_{33} frequency almost perfectly reproduces the frequency shift of the 240-cm^{-1} mode observed experimentally, including the initial upshift measured by the ultrafast uv-pump/vis-probe measurement (*23*). The agreement strongly bolsters our conclusion that the present experiment tracks the structural evolution of *cis*-stilbene during the isomerization through accompanying changes in the vibrational structure. The frequency differences between the

experiment and computation are attributed to the normal coordinate analysis (harmonic approximation) applied to the highly anharmonic S_1 PES.

We thus achieved direct experimental tracking of the continuous structural evolution of a reacting polyatomic molecule by monitoring the evolving frequency of a spectator wave packet. The spectator frequency showed a gradual downshift over the course of the isomerization through a large anharmonic coupling to the isomerization coordinate. This observation arises from the gradual twisting of the olefinic moiety, realized by the out-of-plane motion of the two ethylenic hydrogens with minimal change in the molecular volume. The global molecular rearrangements visualized here lead to the structure at the S_1/S_0 conical intersection, which may be accompanied with further pyramidalization of one ethylenic carbon (*19*). Femtosecond time-domain Raman spectroscopy offers effective probing of complicated multidimensional RC of polyatomic molecules that cannot be tracked by conventional vibrational spectroscopy.

References and Notes

1. M. D. Fayer, *Ultrafast Infrared and Raman Spectroscopy* (Marcel Dekker, New York, 2001).
2. J. Herbst, K. Heyne, R. Diller, *Science* **297**, 822 (2002).
3. P. Kukura, D. W. McCamant, R. A. Mathies, *Annu. Rev. Phys. Chem.* **58**, 461 (2007).
4. P. Kukura, D. W. McCamant, S. Yoon, D. B. Wandschneider, R. A. Mathies, *Science* **310**, 1006 (2005).
5. U. Banin, S. Ruhman, *J. Chem. Phys.* **99**, 9318 (1993).
6. S. Fujiyoshi, S. Takeuchi, T. Tahara, *J. Phys. Chem. A* **107**, 494 (2003).
7. Materials and methods are available as supporting online material on *Science* Online.
8. G. Cerullo *et al.*, *J. Phys. Chem. A* **107**, 8339 (2003).
9. T. Hornung, H. Skenderovic, M. Motzkus, *Chem. Phys. Lett.* **402**, 283 (2005).
10. M. Sumitani, N. Nakashima, K. Yoshihara, *Chem. Phys. Lett.* **68**, 255 (1979).
11. S. Abrash, S. Repinec, R. M. Hochstrasser, *J. Chem. Phys.* **93**, 1041 (1990).
12. D. C. Todd *et al.*, *J. Chem. Phys.* **93**, 8658 (1990).
13. S. T. Repinec, R. J. Sension, A. Z. Szarka, R. M. Hochstrasser, *J. Phys. Chem.* **95**, 10380 (1991).
14. R. J. Sension, A. Z. Szarka, R. M. Hochstrasser, *J. Chem. Phys.* **97**, 5239 (1992).
15. D. C. Todd, G. R. Fleming, *J. Chem. Phys.* **98**, 269 (1993).
16. J. Saltiel, *J. Am. Chem. Soc.* **90**, 6394 (1968).
17. A. B. Myers, R. A. Mathies, *J. Chem. Phys.* **81**, 1552 (1984).
18. H. Petek *et al.*, *J. Phys. Chem.* **94**, 7539 (1990).
19. J. Quenneville, T. J. Martinez, *J. Phys. Chem. A* **107**, 829 (2003).
20. J. M. Rodier, A. B. Myers, *J. Am. Chem. Soc.* **115**, 10791 (1993).
21. The first component is due to instantaneous electronic response of S_1 *cis*-stilbene. The second 70-fs decay corresponds to the $S_n \rightarrow S_1$ internal conversion that occurs after the $S_n \leftarrow S_1$ excitation by the P_2 pulse. The third component decays with the S_1 lifetime. The appearance of this long-lasting component suggests that a fraction of the S_n molecules does not go back to the S_1 state but follows other relaxation routes (permanent bleaching) (*6*).
22. W. M. Kwok *et al.*, *J. Raman Spectrosc.* **34**, 886 (2003).
23. K. Ishii, S. Takeuchi, T. Tahara, *Chem. Phys. Lett.* **398**, 400 (2004).
24. The initial frequency was obtained by the linear fit as the intercept at zero delay, and it was separately evaluated as 243.1 ± 2.3 cm^{-1} in hexadecane and 241.1 ± 1.6 cm^{-1} in methanol. On the average, we determined the common initial frequency as 242 ± 2 cm^{-1}.
25. We made Fourier transform analysis of a beating feature observed in the $S_n \leftarrow S_1$ transient absorption and obtained its power spectrum that shows an intense band corresponding to the 240-cm^{-1} vibration. The center-of-mass frequency of the band was evaluated as 231 ± 3 cm^{-1} in both cyclohexane and methanol.
26. S. Pedersen, L. Banares, A. H. Zewail, *J. Chem. Phys.* **97**, 8801 (1992).
27. H. Iikura, T. Tsuneda, T. Yanai, K. Hirao, *J. Chem. Phys.* **115**, 3540 (2001).
28. R. Improta, F. Santoro, *J. Phys. Chem. A* **109**, 10058 (2005).
29. As already reported, the 240-cm^{-1} vibration exhibits a high Franck-Condon activity in the $S_1 \leftarrow S_0$ transition, indicating that it is a totally symmetric, Raman-active mode showing a large S_0/S_1 potential displacement (*23*). Among the totally symmetric candidate modes in Fig. 4D (ν_{32}, ν_{33}, ν_{34}), the initial frequencies of the ν_{33} and ν_{34} modes are close to 240 cm^{-1}. We found that the S_1/S_0 potential displacement along the ν_{33} mode is largest: Absolute potential gradients at $s = 0$, which reflect the potential displacement, were calculated as 0.0036 (ν_{32}), 0.0076 (ν_{33}), and 0.0033 (ν_{34}) hartree/(bohr·amu$^{1/2}$), respectively (where amu stands for atomic mass unit). Therefore, we assigned the ν_{33} mode to the 240-cm^{-1} vibration observed experimentally.
30. K. Iwata, H. Hamaguchi, *J. Phys. Chem. A* **101**, 632 (1997).

31. This work was supported in part by Grant-in-Aid for Science Research on Priority Area (no. 19056009) from the Ministry of Education, Culture, Sports, Science, and Technology of Japan. S.T. acknowledges financial support by a Grant-in-Aid for Scientific Research (B) (no. 19350017) from the Japan Society for the Promotion of Science (JSPS). T. Tahara and S.R. acknowledge the JSPS invitation fellowship program.

Supporting Online Material

www.sciencemag.org/cgi/content/full/322/5904/1073/DC1
Materials and Methods
References

23 May 2008; accepted 15 September 2008
10.1126/science.1160902

Random Tiling and Topological Defects in a Two-Dimensional Molecular Network

Matthew O. Blunt,[1] James C. Russell,[1] María del Carmen Giménez-López,[2] Juan P. Garrahan,[1] Xiang Lin,[2] Martin Schröder,[2] Neil R. Champness,[2]* Peter H. Beton[1]*

A molecular network that exhibits critical correlations in the spatial order that is characteristic of a random, entropically stabilized, rhombus tiling is described. Specifically, we report a random tiling formed in a two-dimensional molecular network of *p*-terphenyl-3,5,3′,5′-tetracarboxylic acid adsorbed on graphite. The network is stabilized by hexagonal junctions of three, four, five, or six molecules and may be mapped onto a rhombus tiling in which an ordered array of vertices is embedded within a nonperiodic framework with spatial fluctuations in a local order characteristic of an entropically stabilized phase. We identified a topological defect that can propagate through the network, giving rise to a local reordering of molecular tiles and thus to transitions between quasi-degenerate local minima of a complex energy landscape. We draw parallels between the molecular tiling and dynamically arrested systems, such as glasses.

The tiling of surfaces with simple polygons has fascinated scientists, mathematicians, and artists in both ancient and modern cultures. The mathematical rules that govern the formation of periodic tilings, in which tiles are regularly placed on a surface, have been extensively studied and provide the foundation for the classification of crystalline materials. More recently, the discovery of quasi-crystals has inspired great interest in aperiodic tilings, which exhibit symmetries that are not compatible with translational order (*1*–*5*). It is also possible to form tilings in which translational symmetry is absent by using simple tile shapes such as the rhombus with internal angles of 60° and 120°. Rhombus, or lozenge, tilings lead to a particularly rich range of arrangements, which may be periodic, but random nonperiodic tilings are also permitted (*6*, *7*) and have attracted great interest because of their relevance to mixing algorithms (*8*, *9*), antiferromagnetism (*10*, *11*), and entropic models of quasi-crystals (*12*–*15*).

We show that a rhombus tiling may be realized experimentally in a two-dimensional arrangement of organic molecules adsorbed on graphite. Specifically, we studied the molecule *p*-terphenyl-3,5,3′,5′ -tetracarboxylic acid (TPTC) (Fig. 1A), which was synthesized as described in (*16*). The choice of molecule was motivated by the placement of carboxylic acid groups that promote directional intermolecular hydrogen bonding. For TPTC, these groups stabilize two possible relative placements of neighboring molecules, which we refer to as the parallel (Fig. 1B) and arrowhead (Fig. 1C) configurations. Small quantities of a saturated solution of TPTC in nonanoic acid were applied to a freshly cleaved highly oriented pyro-

[1]School of Physics and Astronomy, University of Nottingham, University Park, Nottingham NG7 2RD, UK. [2]School of Chemistry, University of Nottingham, University Park, Nottingham NG7 2RD, UK.

*To whom correspondence should be addressed. E-mail: neil.champness@nottingham.ac.uk (N.R.C.); peter.beton@nottingham.ac.uk (P.H.B.)

lytic graphite (HOPG) substrate, and images of the interface between HOPG and the TPTC solution were acquired by using a scanning tunneling microscope (STM) [see (*16*) for full experimental details]. The samples were prepared and imaged at room temperature. Nonanoic acid has been identified as a suitable solvent by Lackinger *et al.* (*17*, *18*) in their investigations of trimesic and related acids, and the properties of molecular networks stabilized by noncovalent interactions such as hydrogen bonding have been reviewed by a number of authors (*19*–*21*). There have also been recent studies of molecules functionalized with multiple carboxylic acid groups, similar to TPTC (*22*–*24*).

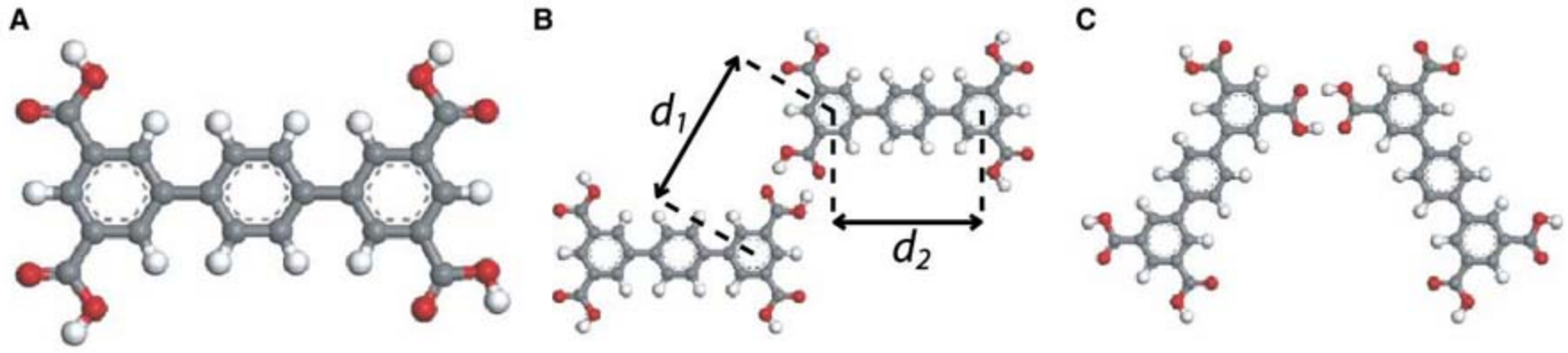

Fig. 1. (**A**) Molecular structure of TPTC. Two possible arrangements for a pair of TPTC molecules linked via a carboxylic acid–carboxylic acid hydrogen bond, (**B**) with the long axes of both molecules parallel to each other, and (**C**) with one molecule rotated by 60° with respect to the other. Marked on (B) are the calculated distances (*16*) between two phenyl rings of different TPTC molecules taken across a carboxylic–carboxylic hydrogen bond (d_1), and the distance between the two end phenyl rings of a single TPTC molecule (d_2).

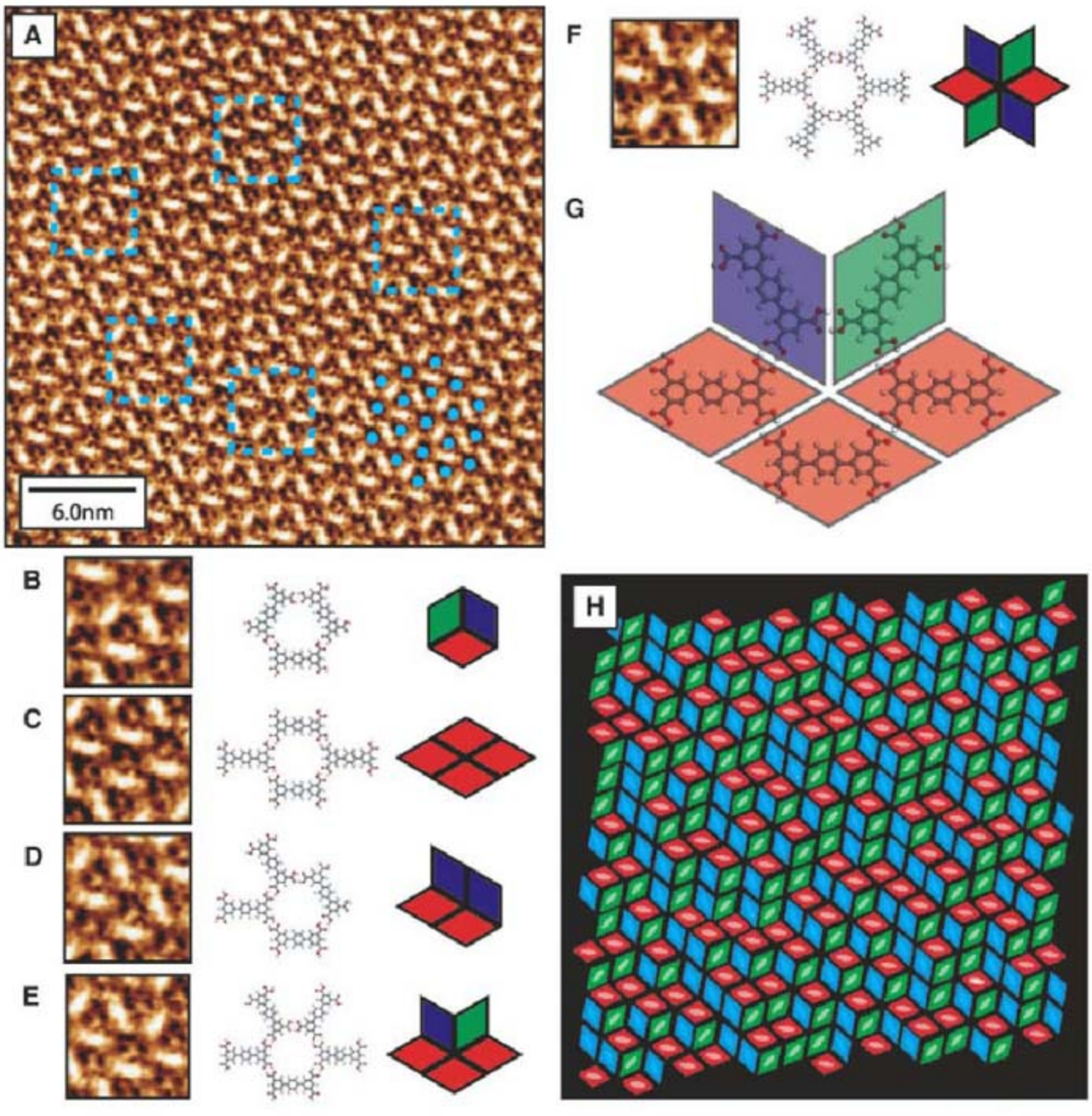

Fig. 2. (**A**) STM image of a typical area of TPTC network at the nonanoic acid/HOPG interface. The group of three phenyl rings constituting the backbone of the TPTC molecules appear as bright rodlike features in the image. The hexagonal orientational order of the structure is highlighted by the group of blue dots in the lower right-hand corner of the image, marking the location of dark contrast regions in the image (depressions/pores in the network). (**B** to **F**) Molecular ball and stick diagrams and tiling representations for the five possible arrangements of TPTC molecules around a network pore. Also shown are magnified STM image examples of each pore type from (A); the locations of the magnified regions are marked in (A) by blue dashed squares. Scanning conditions of (A) were tunneling current (I_t) = 0.015 nA and tip voltage (V_t) = 1200 mV. (**G**) Enlarged version of the molecular arrangement shown in (E). The equivalent tiling representation is shown as a transparent overlay, which highlights the location of the carboxylic acid–carboxylic acid hydrogen bonds at the midpoint of edges between tiles. (**H**) Corresponding tiling representation of (A). The coloration of (H) represents the three possible orientations of rhombi within the tiling (red, green, and blue). Idealized representations of the molecular positions are shown faintly in the tiling.

A typical area of the TPTC network adsorbed on the HOPG surface is shown in Fig. 2A. The terphenyl backbones of the molecules appear as bright rodlike features, and the molecular arrangement is unusual because it exhibits hexagonal orientational order but no translational symmetry. The hexagonal order may be discerned from the array of blue dots overlaid on dark contrast features (corresponding to depressions or pores) in Fig. 2A and, using calibration scans of the graphite substrate, we found that the hexagonal array has a period of 16.6 ± 0.8 Å oriented at an angle of ±6° to the HOPG substrate (*16*). Although the pores are regularly arranged, the molecular network enclosing them is not translationally ordered. Figure 2, B to F, shows that the molecular arrangements enclosing different pores (highlighted areas in Fig. 1A) are hexagons formed by a varying number of molecules.

For example, Fig. 2B shows a hexagon formed by three molecules with edges that alternate between a terphenyl backbone and a carboxylic acid–carboxylic acid junction. Figure 2, C and D, shows two alternative hexagonal arrangements formed by the junction of four molecules with two edges formed by the terphenyl backbone. Similarly, the junction in Fig. 2E is formed by five molecules with one terphenyl edge, and the junction in Fig. 2F is formed by six molecules with no terphenyl edges. The lengths of the hydrogen-bonded and terphenyl edges (equivalent to d_1 and d_2 as defined in Fig. 1B) are calculated to be 9.6 and 8.7 Å [the intermolecular binding energy $E_{HB} = 0.80$ eV is calculated to be the same for the parallel and arrowhead arrangements (*16*)], giving estimated widths of the hexagons in Fig. 2 ranging from 15.8 Å (Fig. 2B) to 16.6 Å (Fig. 2F), which is in good agreement with the measured periodicity. The molecular array shown in Fig. 2A may be built by combining these five structural units in an arrangement that exhibits orientational symmetry but no translational order.

The network may be mapped onto a tiling by replacing each molecule with a rhombus [see (*25*) for another example linking molecular arrays to tiling problems]. Each molecule in the network points along one of three high-symmetry directions, and we have chosen, for clarity, to represent these three molecular orientations as rhombi with different colors. To illustrate the tiling, we have converted each of the hexagonal structural units discussed above into rhombi (Fig. 2). The representations of the junctions in Fig. 2, B to F, correspond to vertices where three, four, five, or six rhombi meet. These diagrams also show that, at a molecular level, the mapping is possible because the intermolecular bonds between neighboring molecules are located at the midpoint of the rhombus edges (Fig. 2G). We suggest that this symmetry is key to identifying other candidate molecules that might form similar networks.

The molecular network displayed in Fig. 2A can be mapped into rhombi, and the resultant tiling is shown in Fig. 2H. The mapping directly accounts for the presence of orientational symmetry combined with an absence of translational order because the rhombus vertices (pores in the STM images) fall on a hexagonal lattice, even though the arrangement of rhombi is not ordered. Thus, we demonstrate that the molecular array is equivalent to a rhombus tiling.

We also observed tiling defects in the form of triangular voids enclosed completely by rhombi (Fig. 3). These voids are topological defects that occur in two states of effective "charge" corresponding to triangles pointing either "up" or "down" and have been considered theoretically but have not previously been observed (*26*–*28*). We observed ~3×10^{-3} defects per adsorbed molecule and may unequivocally distinguish these voids from other less intrinsically interesting defects, such as vacancies. The triangular defects have been observed to propagate through the network, as shown in Fig. 3, C to H. This movement results in a rearrangement of a single molecule (or tile) within the network. Figure 3, C and F, shows a comparison of images before and after such a transition, in which, as expected, effective charge is conserved. The triangular defect undergoes a second movement between Fig. 3, E and G. In our images, this transition appears to be mediated by the temporary presence of an additional species at the defect site, as highlighted in Fig. 3, C and E, possibly an additional TPTC molecule temporarily bound by hydrogen bonding. Although it is difficult to determine the exact details of the atomistic mechanism for defect movement, this sequence of images shows that defect propagation through the network gives rise to a reordering of molecular tiles and facilitates a transition between different local energy minima.

To determine whether the observed rhombus tilings are ordered or random, we followed previous theoretical studies (*10*, *12*) and introduced an effective height $h(x,y)$ at each vertex (x,y). The height was calculated with the scheme shown in Fig. 4A, in which a displacement along a rhombus edge leads to a change in height of ±1. By arbitrarily choosing an origin with zero height, it is possible to define $h(x,y)$ for all vertices of a perfect (defect-free) tiling. Within this scheme, a tiling may be visually considered as a perspective of the surface of a simple cubic lattice when viewed along a (111) direction. More formally, the rhombus tiling is equivalent to the projection of an irregular surface of a three-dimensional simple cubic crystal onto a (111) plane of the cubic lattice. A map of effective height of the STM image (Fig. 2A) is shown in Fig. 4C.

Within the random tiling hypothesis (*11*), the tilings may be analyzed by introducing an effective free energy G, which, assuming that all vertex types (shown in Fig. 2) are degenerate, is determined entirely by an entropic contribution and is given by $G = (K_o/2)\int|\nabla h|^2\, dxdy$. This contribution is equivalent to the energy of a deformed surface with elastic constant K_o. The gradient ∇h corresponds to the projection in the (x,y) plane of the normal to the representative surface. The tilings that are generated by this free energy have a height representation for which $\langle \nabla h \rangle = 0$, that is, a surface which on average is flat and par-

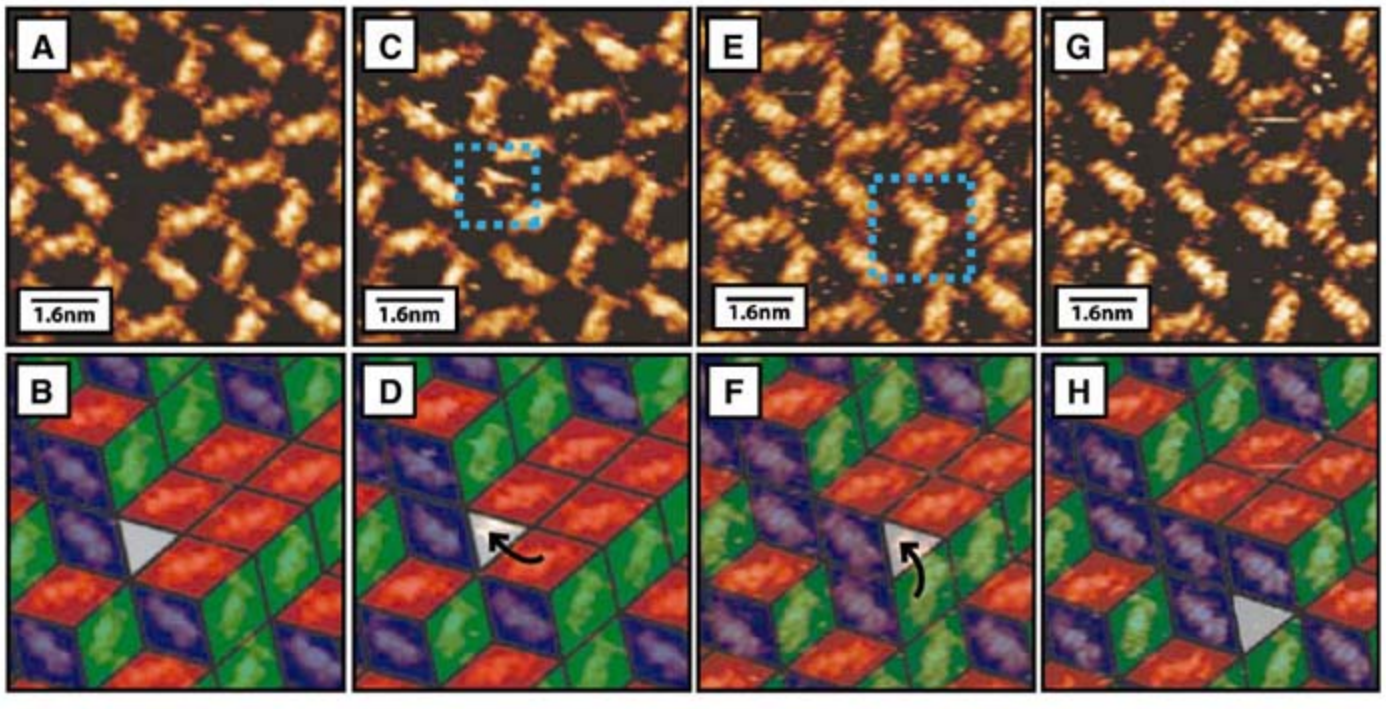

Fig. 3. (**A**, **C**, **E**, and **G**) STM images showing two separate movements of a single defect through the network structure. (**B**, **D**, **F**, and **H**) Tiling representation of the network structure during the defect motion. The effective rearrangements of rhombi in the tiling are marked by the black arrows in (D) and (F). Transient image artifacts observed within the defect site before defect motion are highlighted by blue dashed squares [(C) and (E)]. Scanning conditions for all images were I_t = 0.021 nA and V_t = 1200 mV.

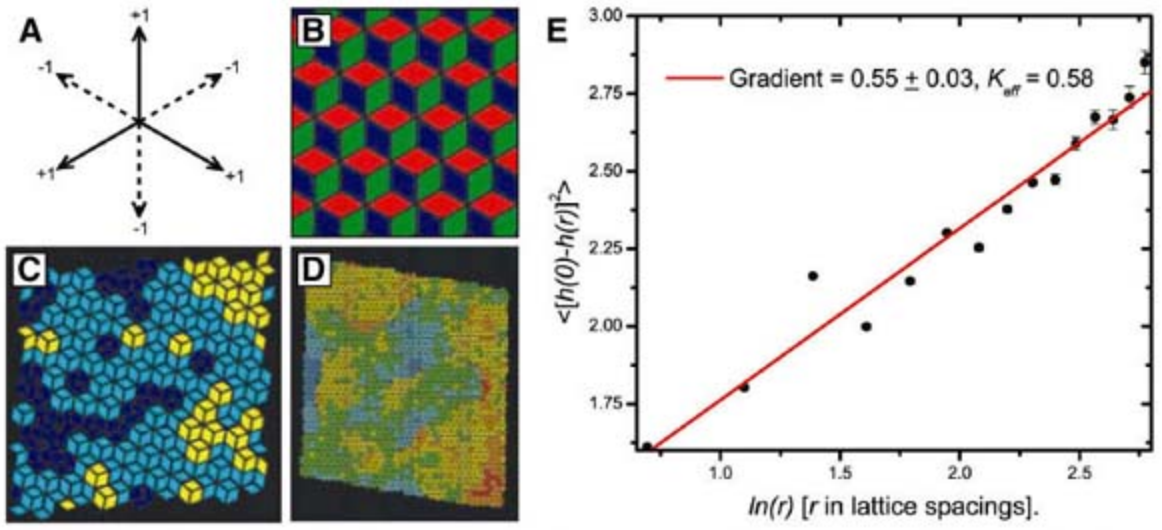

Fig. 4. **(A)** Scheme for evaluating height function of a tiling. A displacement from a vertex along three of the possible directions leads to an increase in height by 1 as shown; a displacement along the other three directions leads to a decrease by 1. **(B)** A schematic showing a flat undeformed representative surface to be compared with the (111) surface of a simple cubic crystal. **(C)** Height representation of tiling in Fig. 2. Here the height of a tile is calculated as the average over its four vertices; different heights are represented as different colors. **(D)** Height map of one of the large area scans (100 nm by 100 nm) used to generate correlation function [see (*16*) for more details]. **(E)** Dependence of correlation on separation demonstrating logarithmic dependence. Scanning conditions for all images were I_t = 0.015 nA and V_t = 1200 mV.

allel to a (111) plane of the projected cubic lattice, which is equivalent to a requirement that equal numbers of tiles are oriented in each of the three possible directions. Fluctuations in height with wavevector $\underline{k}$ are expected with a Fourier spectrum $h(\underline{k}) \propto K_o^{-1}|\underline{k}|^{-2}$. In two dimensions, this spectrum leads to logarithmic spatial correlations in $h(x,y)$, $C(r) = \langle[h(0) - h(r)]^2\rangle = (\pi K_o)^{-1} \ln(r) + c$, where c is a constant and, for the maximally random rhombus tiling, $K_o = \pi/9$ (*10*, *12*).

We calculated the height correlation function $C(r)$ from STM images that had been converted to a height representation (Fig. 4D). The fraction of tiles pointing in the three directions is in the ratio 1:1:1, within statistical error, and thus the condition $\langle\nabla h\rangle = 0$ is satisfied [see (*16*) for tile maps and ratios of tile orientations]. It is not possible to solely specify $h(x,y)$ in the presence of triangular void defects because the line integral of $h(x,y)$ along a closed path around a triangular void gives a nonzero value corresponding to the winding number of the defect (in this case, ±3). However, it is possible to unambiguously calculate the contributions to the height correlation function in regions that do not enclose defects. Our method for calculating $C(r)$ is based on this approach and provides reliable data for $r \leq r_d$, the average defect separation.

As shown in Fig. 4E, the measured $C(r)$ has the expected logarithmic dependence on r, corresponding to the critical correlations of a random rhombus tiling (*12*). The effective elasticity of the tiling may be extracted from the prefactor of the logarithm. We find $K_{eff} = 0.58 \pm 0.03$, or equivalently $K_{eff}/K_o \sim 1.7$.

The enhancement of the elastic constant over the expected value K_o is explained as a breaking of the exact degeneracy in local bonding arrangements, with a small energetic preference for the arrowhead (Fig. 1C) configuration. This difference in energy results in an energy cost for vertices that have neighboring tiles in the parallel configuration (Fig. 2, C to E). These vertices [which are not present on the idealized undeformed (111) representative surface, for which molecules are exclusively in the arrowhead arrangement (Fig. 4B)] are associated with local changes in height $\nabla h \neq 0$, leading to an energetic contribution to the free energy in addition to the purely entropic term discussed above. These effects lead to an increase in the effective elastic constant K_{eff} in G.

This explanation is consistent with results by Alet *et al.* (*29*) for closed packed dimers on the square lattice with aligning interactions, in which there is a critical phase with an effective elasticity that increases with increasing interaction strength Δ [and an eventual phase transition to an ordered phase for $\Delta \sim kT$ (T, temperature), where other terms become relevant in the free energy G (*29*)]. In the context of our experiments, Δ characterizes the energy difference between the parallel and arrowhead configurations. Our finding of logarithmic correlations with K_{eff} close to K_o, to within a factor 2, confirms that our system is in the random tiling regime and therefore $\Delta < kT$ (0.03 eV). This very small value of energy, comparable with the uncertainty in our calculation of E_{HB}, highlights the delicate balance required for entropically stabilized randomness in the rhombus tiling.

Although the above analysis of the spatial distribution of tiles is based on the equilibrium free energy G, it is clear that the tilings are frozen, with minimal temporal evolution, in one local minimum of a complex energy landscape. The system is dynamically arrested, similar to a glass, and all tile movements are activated with an energy cost that is expected to scale with the number of intermolecular hydrogen bonds that must be broken. Triangular defects, which mediate the only tile rearrangements that have been experimentally observed, have the lowest activation barrier because only three bonds must be broken in order to move a molecule directly adjacent to a defect. Other tile rearrangements, such as the 60° rotation of the hexagonal unit in Fig. 2B, often considered in the context of mixing algorithms for perfect (defect-free) random tilings (*8*), require six bonds to be broken and would be expected to be exponentially suppressed. The observation of the propagation of localized defects as a mechanism for transitions between different local energy minima is highly reminiscent of dynamically facilitated models of glass formers (*30*, *31*). Our results demonstrate the potential of molecular tilings as model systems for the study of glasses and provide an interesting alternative to the random molecular networks recently identified by Otero *et al.* as glassy systems (*32*).

Our results show that, once formed, tilings are trapped in one of a large number of quasi-degenerate locally stable states that can rearrange through defect migration. Overall, the connection between rhombus tiling and molecular architecture, through the approximate equality $d_1 \sim d_2$, leads to design rules for a general class of analogous molecular networks in two and three dimensions that can provide novel model systems for the study of random structural arrangements and dynamically arrested materials.

References and Notes

1. D. Shechtman, I. Blech, G. Gratias, J. W. Cahn, *Phys. Rev. Lett.* **53**, 1951 (1984).
2. D. Levine, P. J. Steinhardt, *Phys. Rev. Lett.* **53**, 2477 (1984).
3. G. Onoda, P. J. Steinhardt, D. J. DiVincenzo, J. E. S. Socolar, *Phys. Rev. Lett.* **60**, 2653 (1988).
4. J. Ledieu *et al.*, *Phys. Rev. Lett.* **92**, 135507 (2004).
5. J. Yuhara *et al.*, *Phys. Rev. B* **70**, 024203 (2004).
6. M. E. Fisher, *Phys. Rev.* **124**, 1664 (1961).
7. P. Kasteleyn, *J. Math. Phys.* **4**, 287 (1963).
8. D. B. Wilson, *Ann. Appl. Probab.* **14**, 274 (2004).
9. H. Cohn, R. Kenyon, J. Propp, *J. Am. Math. Soc.* **14**, 297 (2001).
10. H. W. J. Blote, H. J. Hilhorst, *J. Phys. A* **15**, L631 (1982).
11. R. Moessner, S. L. Sondhi, E. Fradkin, *Phys. Rev. B* **65**, 024504 (2002).
12. C. L. Henley, in *Quasicrystals, the State of the Art*, D. P. DiVencenzo, P. J. Steinhardt, Eds. (World Scientific, Singapore, 1999), p. 459.
13. M. Widom, D. P. Deng, C. L. Henley, *Phys. Rev. Lett.* **63**, 310 (1989).
14. N. Destainville, *Phys. Rev. Lett.* **88**, 030601 (2002).
15. A. S. Keys, S. C. Glotzer, *Phys. Rev. Lett.* **99**, 235503 (2007).
16. Materials and methods and additional data are available as supporting material on *Science* Online.
17. M. Lackinger, S. Griessl, W. A. Heckl, M. Hietschold, G. W. Flynn, *Langmuir* **21**, 4984 (2005).
18. S. J. H. Griessl *et al.*, *Langmuir* **20**, 9403 (2004).
19. S. de Feyter, F. C. de Schryver, *J. Phys. Chem. B* **109**, 4290 (2005).
20. J. V. Barth, G. Costantini, K. Kern, *Nature* **437**, 671 (2005).
21. F. Rosei *et al.*, *Prog. Surf. Sci.* **71**, 95 (2003).
22. H. Zhou *et al.*, *J. Am. Chem. Soc.* **129**, 13774 (2007).
23. M. Blunt *et al.*, *Chem. Commun.* 2304 (2008).
24. M. Li *et al.*, *Angew. Chem. Int. Ed.* **47**, 6717 (2008).
25. M. Pivetta, M. C. Blum, F. Patthey, W. D. Schneider, *Angew. Chem. Int. Ed.* **47**, 1076 (2008).
26. M. E. Fisher, J. Stephenson, *Phys. Rev.* **132**, 1411 (1963).

27. J. Linde, C. Moore, M. G. Nordahl, *Discrete Mathematics and Theoretical Computer Science Proceedings AA* (DM-CCG) *23* (2001).
28. W. Krauth, R. Moessner, *Phys. Rev. B* **67**, 064503 (2003).
29. F. Alet *et al.*, *Phys. Rev. Lett.* **94**, 235702 (2005).
30. G. H. Fredrickson, H. C. Andersen, *Phys. Rev. Lett.* **53**, 1244 (1984).
31. J. P. Garrahan, D. Chandler, *Proc. Natl. Acad. Sci. U.S.A.* **100**, 9710 (2003).
32. R. Otero *et al.*, *Science* **319**, 312 (2008).
33. We thank the UK Engineering and Physical Sciences Research Council (EPSRC) for financial support under grant EP/D048761/01. J.P.G. was supported by EPSRC grant GR/S54074/01. M.S. acknowledges receipt of a Royal Society Wolfson Merit Award.

Supporting Online Material
www.sciencemag.org/cgi/content/full/322/5904/1077/DC1
Materials and Methods
Figs. S1 to S4
References

16 July 2008; accepted 6 October 2008
10.1126/science.1163338

Observing the Creation of Electronic Feshbach Resonances in Soft X-ray–Induced O_2 Dissociation

Arvinder S. Sandhu,[1]*† Etienne Gagnon,[1]* Robin Santra,[2,3] Vandana Sharma,[1] Wen Li,[1] Phay Ho,[2] Predrag Ranitovic,[4] C. Lewis Cocke,[4] Margaret M. Murnane,[1]‡ Henry C. Kapteyn[1]

When an atom or molecule is ionized by an x-ray, highly excited states can be created that then decay, or autoionize, by ejecting a second electron from the ion. We found that autoionization after soft x-ray photoionization of molecular oxygen follows a complex multistep process. By interrupting the autoionization process with a short laser pulse, we showed that autoionization cannot occur until the internuclear separation of the fragments is greater than approximately 30 angstroms. As the ion and excited neutral atom separated, we directly observed the transformation of electronically bound states of the molecular ion into Feshbach resonances of the neutral oxygen atom that are characterized by both positive and negative binding energies. States with negative binding energies have not previously been predicted or observed in neutral atoms.

The ability to reveal fast correlated electronic dynamics with ultrafast x-rays has attracted considerable interest in recent years. In general, some of the fastest electronic processes involve highly excited states. Autoionization after photoionization of an electron from an atom, molecule, or solid is a good example of one such process (*1*–*8*). Autoionization is an important electronic many-body problem in molecules, and the electrons and ions produced also contribute to radiation damage in materials and biological systems (*9*). In the autoionization of a deep inner-shell hole, an electron from a higher energy level fills the hole, while a second outer (Auger) electron is ejected, carrying away excess energy. Auger decay from a deep inner-shell hole is always energetically allowed, both in isolated atoms and molecules. In this case, the molecular environment generally plays a minor role. In contrast, autoionization of an inner-valence vacancy in an isolated atom is often energetically forbidden. For example, the $2s^1 2p^4\ ^2P$ inner-valence state of O^+ lies 40 eV above the ground state of atomic oxygen but 9 eV below the O^{2+} ground state and can therefore only decay radiatively; that is, by emitting a photon. However, in polyatomic systems, autoionization after inner-valence ionization can be energetically allowed because the molecular environment can play a role. Because the two final-state charges in a molecular dication do not have to sit on one atom, the Coulomb repulsion between the holes is reduced, and thus the double ionization threshold is lowered.

Interatomic Coulombic decay (ICD) in the Ne dimer, for instance, is a prominent example in which the molecular environment plays a major role in autoionization and has received much recent attention (*1*, *2*, *10*). In ICD in Ne, autoionization of a 2s hole relies on energy transfer between the two Ne atoms and thus preferentially takes place near the equilibrium separation of the atoms of the neutral Ne dimer. Molecular oxygen (O_2) can also autoionize after photoionization in the inner-valence region (*4*–*6*). However, O_2 does not follow the paradigm provided by ICD, in which autoionization occurs when the atoms are in proximity. Rather, Feifel *et al.* (*4*) performed a high-resolution coincident electron study of O_2 and concluded that the atomiclike character of the autoionization spectrum indicates that the decay takes place at large interatomic distances, which is in stark contrast to ICD. However, these experiments did not have any time resolution: Without the ability to observe intermediate states, it was not possible to uncover the mechanism for autoionization to fully understand what was happening.

In this work, we irradiated an O_2 molecule with a few-femtosecond x-ray pulse to create superexcited states of the O_2^+ molecular ion. We then used an ultrafast laser pulse to follow how this superexcited state evolves into an autoionizing state. We achieved this by interrupting the autoionization with an ultrafast laser pulse at different times during the process. First, we found that autoionization cannot occur until the molecular fragments are well-separated, by distances of >30 Å. Second, we found that the autoionizing state forms 300 fs after x-ray irradiation and emerges as a negative binding-energy Feshbach resonance. The use of ultrafast x-rays and lasers (*11*), in combination with a triple-coincidence detection scheme, allowed us to directly observe the onset of these negative binding-energy Feshbach autoionizing states. Before this work, the existence of negative binding-energy states in neutral atoms was not anticipated. Third, by providing an explanation for the atomic nature of the autoionization lines observed in O_2, we were able to highlight the dramatic difference between the roles of the molecular environment in ICD in van der Waals dimers and molecular autoionization, in which the presence of a molecular field can suppress, rather than enhance, autoionization. Finally, we showed that we can manipulate superheated, metastable, autoionizing states before they decay and actively influence, with a strong field, whether a superexcited state will have the opportunity to decay or not. This capability raises the possibility of coherent manipulation of highly excited quantum states, even when their energies lie above the ionization potential. Autoionization after soft x-ray photoionization of O_2 is thus a much more complex multi-step process than in the case of N_2, with which in recent studies we used an ultrafast soft x-ray pump combined with an infrared probe to study electron shakeup processes (*12*, *13*).

Several studies have reported the existence of negative binding energy states in multiply charged molecular ions (anions) (*14*–*16*). A particular electronic state is considered to have a negative binding energy when the kinetic energy of an ejected photoelectron is greater than the single-photon energy used for the ionization step. This means that the electronic state must be higher in energy than the ionization channel being considered. A state with negative binding energy must therefore be metastable. The repulsive Coulomb barrier in multiply charged anions supports long-lived shape resonances (metastable states that decay by tunneling through a potential barrier), which because of their long lifetime are easy to detect experimentally. To date, states with negative electron–binding energy were thought to be

[1]JILA, University of Colorado at Boulder, Boulder, CO 80309, USA. [2]Argonne National Laboratory, Argonne, IL 60439, USA. [3]Department of Physics, University of Chicago, Chicago, IL 60637, USA. [4]J. R. MacDonald Lab, Department of Physics, Kansas State University, Manhattan, KS 66506, USA.

*These authors contributed equally to this work.
†Present address: Department of Physics, University of Arizona, Tucson, AZ 85721–0081, USA.
‡To whom correspondence should be addressed. E-mail: margaret.murnane@colorado.edu

a feature only of multiply charged anions because of the presence of a repulsive Coulomb barrier.

Feshbach resonances occur in compound systems such as atoms, molecules, nuclei, or quarkonia, when a bound state in a closed channel can decay into a continuum state in an open channel via interchannel coupling. The nature of the channels and the nature of the interchannel coupling depend on the system under consideration. If at least one of the partners in a collision process, for example, is itself a compound system, one cannot necessarily characterize a collision entirely in terms of the relative motion of two collision partners within an effective collision potential because the internal degrees of freedom of the systems may be dynamically involved in the collision. Feshbach resonances have been known since Herman Feshbach formalized them in the 1950s (*17*). Initially, the Feshbach resonance picture was used to describe nuclear collisions. However, more generally any autoionizing state generated by removing an inner-shell electron is a Feshbach resonance, and therefore these states underlie Auger, Coster-Kronig, or ICD decay. In recent years, Feshbach resonances have been exploited in ultracold collisions, in which the collision energy is very small (*18*, *19*). In these systems, the relative position of the open and closed channels can be adjusted by using a variable magnetic field. This provides a simple knob to control the collisional properties of an ultracold gas.

The experimental setup and schematic of the molecular autoionization process are shown in Fig. 1. The output from an ultrafast Ti:sapphire amplifier system producing ~2-mJ pulses with ~30 fs duration, at a repetition rate of 2 kHz, was split into pump and probe beams. (*12*, *13*) The pump beam (~1.2 mJ) was used to generate an ultrashort (<10 fs) soft x-ray pump beam with a photon energy of 42.7 eV (full width at half maximum ≈ 1.5 eV) through high-order harmonic upconversion. The net photon flux, after filtering out the visible laser and selecting a single harmonic with a pair of multilayer mirrors, was ~10^6 photons per pulse or 2×10^9 photons/s. The probe beam (~0.8 mJ) was time-delayed and recombined with the soft x-ray pump beam in the interaction region, which provided a means to dynamically probe the autoionization process. This infrared (IR) probe beam passed through an optical chopper with a 50% duty cycle, which allowed us to normalize our data on a shot-to-shot basis. The IR probe beam was focused onto the O_2 sample with a 75-cm lens to an intensity of 4.9×10^{12} W/cm^2. The target O_2 gas was cooled and confined with a supersonic jet expansion employing a 30-μm nozzle. The cold supersonic portion of the jet was selected using a 300-μm skimmer placed ~13 mm from the gas nozzle. The gas density in the interaction region was estimated to be ~10^{11} to 10^{12} cm^{-3}. A cold-target recoil ion momentum spectroscopy (COLTRIMS)–based reaction microscope collected reaction fragments with high efficiency (solid angle ~4π) for both electrons and ions for each laser shot.

Figure 2 shows electron and ion kinetic energy spectra acquired with our coincident ion/electron detectors for the case of soft x-ray illumination of O_2. For these spectra, an electron was detected in coincidence with two O^+ ions. By requiring that the two ions have nonzero kinetic energy release and zero total momentum, we ensured that both ions came from the same molecule. The broad feature centered at ≈1.8 eV in the electron-energy spectrum in Fig. 2 corresponded predominantly to the photoelectron (one-photon single ionization) and to electrons produced via direct one-photon double ionization. The width of this feature was partly determined by the distribution of binding energies of the various autoionizing states of O_2^+ that are populated (*4*). More electronic states are excited than one might expect based on the number of initially occupied orbitals. This is an example of the breakdown of the molecular orbital picture for inner-valence electrons (*20*).

The electron-energy peak appearing at ≈0.5 eV is consistent with the A1 and A2 autoionization lines of O_2 that were identified by Feifel *et al*. (*4*). (Other, less prominent autoionization lines are merged with the photoelectron

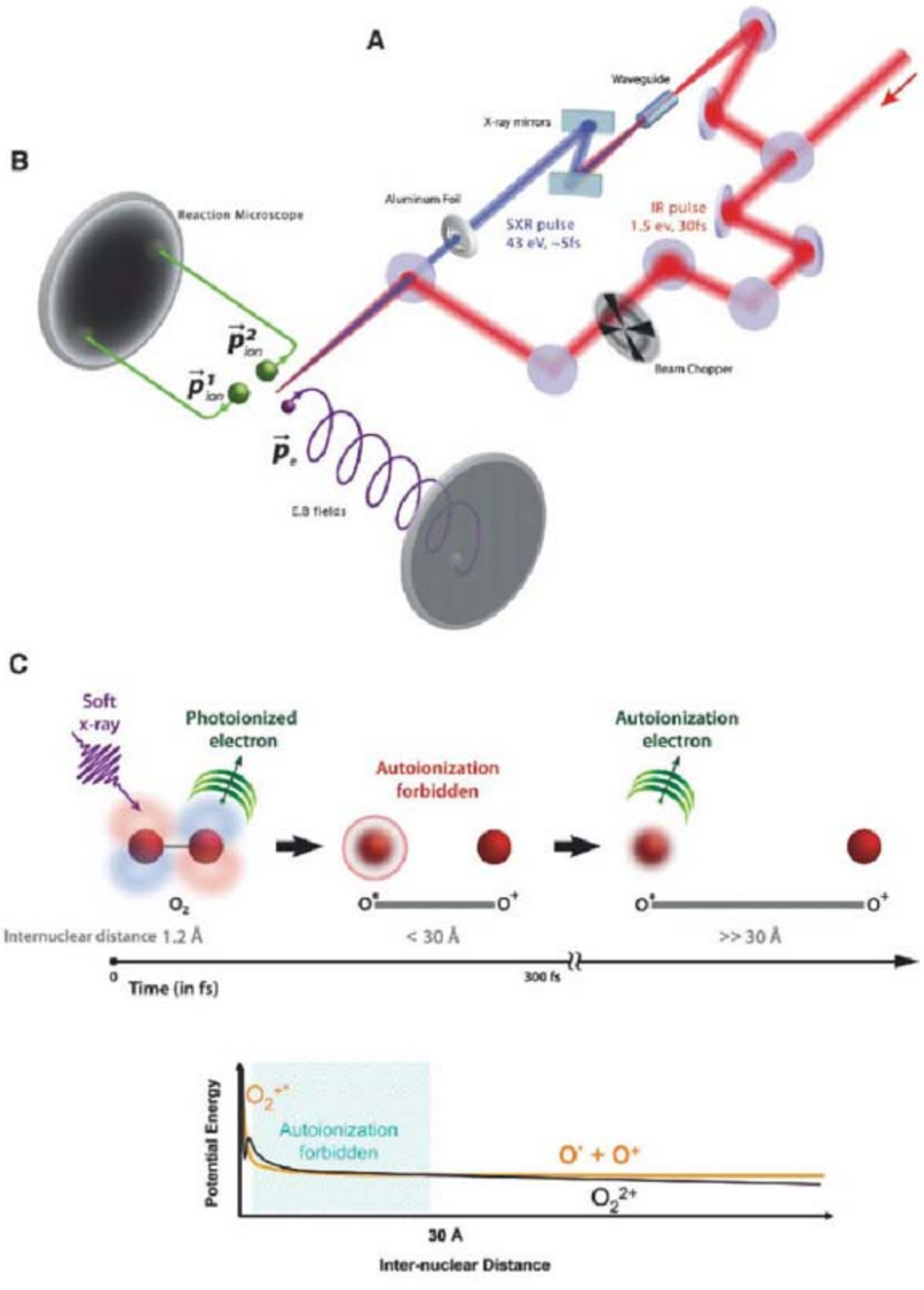

Fig. 1. (**A**) Schematic of the experimental setup in which a soft x-ray beam photoionizes the O_2 molecule while an IR probe beam interrupts the autoionization in order to follow the dynamics. E,B fields, electric and magnetic fields, respectively; SXR, soft x-ray beam. (**B**) COLTRIMS reaction microscope. (**C**) Schematic of the multistep photoionization, dissociation, and autoionization of O_2. Autoionization is forbidden until the autoionizing state emerges as a negative-binding energy Feshbach resonance at internuclear separations of 30 Å or greater.

distribution.) As pointed out in (*4*), the A1 and A2 autoionization lines observed are so narrow that the electronic decay process must be taking place in the dissociation limit, in which the atomic fragments are well separated. Specifically, the A1 line corresponds to the $2s^22p^3(^2D^o)3p^1\ ^3D$ state of atomic oxygen. In this state, which is 0.43 eV above the ground state of O^+ $2s^22p^3(^4S^o)$, the 3p electron is bound to the $2s^22p^3\ ^2D^o$ excited-state ion core (Fig. 3B). This $2s^22p^3\ ^2D^o$ excited state of O^+ is a closed channel for autoionization because this transition is energetically forbidden; there is simply insufficient energy for the autoionizing electron to be ejected, leaving behind O^+ in the first excited state. Thus, the $2s^22p^3\ ^4S^o$ ground state of O^+ is the only open channel into which the autoionizing state can decay. The necessary change in the electronic configuration of the ion core (channel coupling) that must accompany autoionization is mediated by the electron-electron and spin-orbit interactions; in the absence of spin-orbit coupling, that is, when the total orbital angular momentum L and the total spin S are good quantum numbers, autoionization would be forbidden. As described above, relaxation via channel coupling is precisely the required characteristic of a Feshbach resonance. The A2 line corresponds to the $2s^22p^3(^2D^o)3p\ ^3F$ [autoionization LS-allowed] and $2s^22p^3(^2P^o)3s\ ^3P^o$ (autoionization LS-forbidden) states of atomic oxygen. They lie 0.48 and 0.51 eV, respectively, above the O^+ ground state.

The kinetic energy release (KER) of the two detected O^+ ions shown in Fig. 2 was obtained by considering only those counts that were associated with the autoionization electrons (electrons with energies between 0 and 1 eV in Fig. 2). The structure of this KER spectrum [see (*5*) for a similar measurement] can be understood using the O_2^+ electron-binding energies (*4*), the atomic autoionization electron energies, and the O_2^{2+} dissociation limits (*21*). These parameters allow the assignment of the strongest KER peaks between 4.9 and 7.5 eV in Fig. 2 to events associated with the quasiatomic A1 and A2 autoionization lines. Therefore, after O_2 is ionized by a 43-eV soft x-ray photon, a highly excited O_2^{+*} is formed. The molecular cation dissociates into an ion O^+ and an excited oxygen atom O*. From the narrow observed autoionization lines (*4*), the superexcited oxygen atom autoionizes only after dissociation, resulting in a second O^+ ion.

This brings us to an obvious question: Why does autoionization not happen at short interatomic distances? Because the presence of a neighboring ion breaks the spherical symmetry, there should be no need for spin-orbit coupling in order to drive LS-forbidden autoionization. Autoionization could then conceivably be as fast as molecular dissociation. An answer to this question is suggested by Fig. 3, which shows a few of the lowest-lying potential energy curves of O_2^{2+} [see (*21*) for further curves] as well as the autoionizing state (orange line). We calculated the potential energy curves using the ab initio program package COLUMBUS (*22*–*24*), employing the high-quality Gaussian basis set cc-pV5Z (*25*) in combination with a multiconfiguration self-consistent-field calculation followed by a multireference configuration-interaction calculation. In Fig. 3A, we plot the region near the Franck-Condon window (1.16 to 1.27 Å) with respect to the vibrational ground state of O_2. At a photon energy of 42.7 ± 0.75 eV, a typical photoelectron energy of ≈2 eV or higher (Fig. 2) implies that, within the Franck-Condon window, the majority of associated O_2^+ states can only decay into the $X^1\Sigma_g^+$ channel. The corresponding predissociating vibrational states of O_2^{2+} below

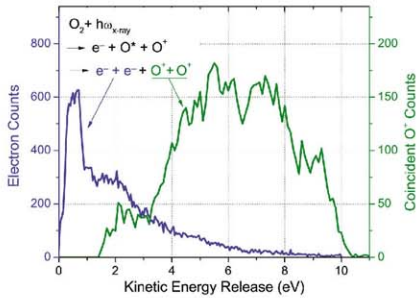

Fig. 2. Coincident electron and ion (O^+ + O^+) kinetic energy spectra in the presence of the soft x-ray field alone (triple coincidence detection). The detected electrons include the autoionizing electrons (lower energy, ≈0.5 eV) and the photoelectrons (higher energy). $h\omega_{x\text{-ray}}$, soft x-ray photo energy.

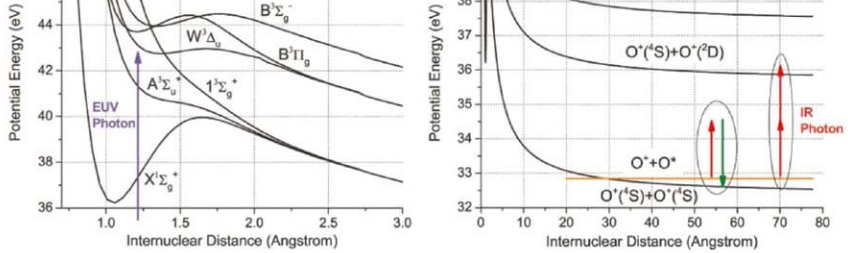

Fig. 3. (A) Potential energy curves of O_2^{2+} for short internuclear distances near the Franck-Condon window. Each curve is labeled by conventional spectroscopic notation that indicates the symmetry of the state. **(B)** Potential energy curves [same as in (A)] shown for large internuclear distances. The orange line shows the energy of the ground-state oxygen ion O^+ ($^4S^o$) plus an autoionizing oxygen atom (corresponding to the A2 autoionizing line). Absorption of a single IR photon (red arrows) ionizes the Feshbach autoionizing state, leaving the system in the ground state of O_2^{2+}. This process results in a photoelectron energy (green arrow) greater than the incident IR photon energy.

vibrational levels $v = 13$ are very long-lived (*26*) and do not contribute to the coincidence signal considered here. The known potential energy curves of O_2^+ in the inner-valence regime are all highly repulsive (*27*). Therefore, unless autoionization into quasi-bound states on the X curve has already taken place (if spin-allowed), the potential energy of O_2^+ would be expected to drop below all O_2^{2+} curves. Fast dissociation would therefore occur, and the O_2^+ curves would then become essentially flat. However, autoionization will still remain energetically forbidden until the O_2^+ curves (Fig. 3B, orange line) cross one or more O_2^{2+} curves for a second time. As shown in Fig. 3B, in the case of the O_2^+ potential energy curves correlating to a ground-state O^+ ion and an excited oxygen atom that are associated, for example, with the A2 autoionization line, the crossing point with the $O^+(^4S^o) + O^+(^4S^o)$ curve lies at ≈30 Å. Only for interatomic distances greater than this is autoionization energetically allowed. In view of the ion KER shown in Fig. 2, for these ion velocities it should take between 220 and 280 fs to reach this crossing point.

We have experimental and theoretical [see supporting online material (SOM) text] evidence that this scenario is correct. Figure 4 displays electron-energy spectra, measured in coincidence with two O^+ ions, for various time delays between the soft x-ray pump and IR probe pulses. At time delays smaller than 300 fs, the coincidence rate is similar to the soft x-ray–only case. However, the A1/A2 autoionization feature at low electron energies is absent. At early time delays, the IR pulse suppresses atomic autoionization partly by producing dissociative O_2^{2+} at short interatomic distance, thus giving rise to a shift of the KER toward larger values, and partly by transferring population to states that do not contribute to the coincidence signal (SOM text and figs. S1 and S2). Two new features begin to appear at time delays around 300 fs: a peak at ≈2 eV of electron energy and a peak near zero electron energy. We interpret these features in terms of the mechanisms indicated in Fig. 3B. After the dissociation of O_2^{+*} has reached the crossing point at internuclear separations around 30 Å as described earlier (for each electronic state there is a somewhat different crossing point), we have an O ion and an excited oxygen atom born into a Feshbach resonance state. Absorption of a single IR photon of energy 1.55 eV from this Feshbach state liberates a photoelectron of energy ≈2 eV, which shows that this state has a negative binding energy with respect to the ground state of O^+. Two-photon absorption yields a photoelectron energy of ≈0.1 eV, corresponding to excitation to the first excited state of O^+, as shown in Fig. 3B. The width of the observed features is largely determined by the resolution of our apparatus and by the bandwidth of our laser. There may also be a contribution from above-threshold ionization.

The negative and positive binding-energy features move to slightly higher energy at longer time delays. This is due to the fact that the O_2^+ potential energy curves on which the nuclear wave packet travels before IR ionization are flat, whereas the O_2^{2+} potential energy curves are influenced by the ion-ion Coulomb repulsion (Fig. 3B). At time delays of 1000 fs, a small shoulder appears in the electron-energy spectra around ≈0.5 eV, where the soft x-ray–only spectra are peaked. As mentioned earlier, autoionization of one of the two resonances that contribute to the A2 line is LS-allowed, with an expected lifetime of the order of 1 ps (*28*). It is probable that this shoulder is due to LS-allowed autoionization preceding the IR probe pulse. The lifetime of resonances whose autoionization is LS-forbidden is expected to be on the order of 1 ns, in competition with radiative decay. This translates to an autoionization efficiency of less than unity. The IR probe efficiently ionizes the Feshbach resonance states, thus leading to a higher coincidence rate than in the soft x-ray–only case, as confirmed in Fig. 4.

Given our findings, it is interesting to compare autoionization in van der Waals dimers with the same process in small covalently bound molecules. Both Ne_2 and O_2 can in principle autoionize within the Franck-Condon window. The reason is the same in both cases: It takes less energy to form a dication with one positive charge on one atom and a second positive charge on the other atom than it takes to form a dication with two positive charges localized on a single atom. However, the real difference between the Ne dimer and O_2 is the following: The inner-valence potential energy curves of the neon dimer cation are very flat; therefore, the Ne atoms do not separate until interatomic Coulombic decay has taken place because dissociation of the inner-

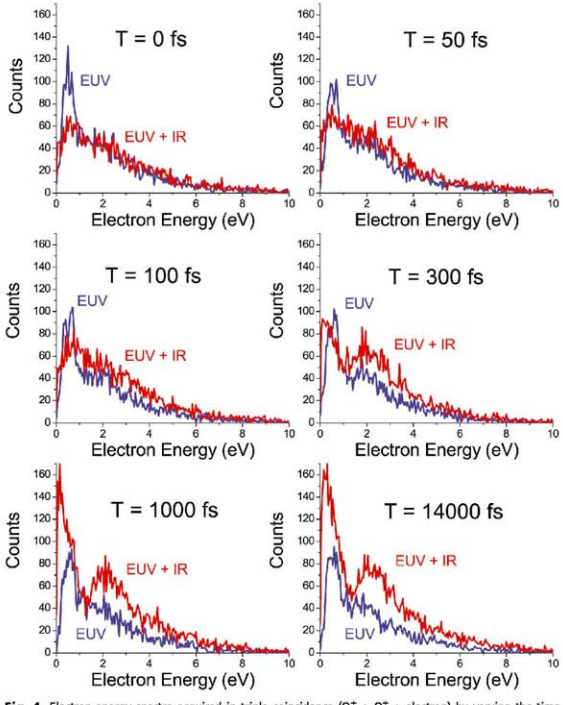

Fig. 4. Electron-energy spectra acquired in triple coincidence ($O^+ + O^+$ + electron) by varying the time delay (*T*) between the soft x-ray pump and IR probe pulses. Soft x-ray–only spectra are shown for comparison. Near time zero, the presence of the IR field suppresses autoionization. For times >300 fs, the presence of the IR field enhances ionization by ionizing the Feshbach resonance before autoionization or radiative decay has time to occur (Fig. 3B).

valence–ionized Ne dimer is slow in comparison to ICD. The flatness of the inner-valence potential energy curves, which enables ICD at essentially all interatomic distances and prevents ultrafast dissociation, is specific to van der Waals systems. In real molecules such as O_2, electron-correlation effects are stronger: The adiabatic potential energy curves in the inner-valence regime are not flat and have many avoided crossings associated with steep dissociative curves. Real molecules can rapidly dissociate and convert electronic energy into kinetic energy of the dissociating fragments.

Finally, without triple-coincidence COLTRIMS experiments to locate the curve-crossing region and moment of onset of the Feshbach autoionizing state, accurate modeling of these superexcited states would not have been possible. Generally, electronic-structure methods, even for excited states, have made substantial progress. However, the inner-valence regime remains challenging because of the large number of electronic states involved and because of the considerable role that electronic many-body effects play in this highly excited energy regime.

We have uncovered the onset of an electronic Feshbach resonance and the existence of negative binding-energy states in neutral atoms. We show that it is possible to actively manipulate superexcited states above the ionization potential by interrupting autoionization with a strong femtosecond laser field. These findings should be applicable to autoionizing states in small molecules.

References and Notes

1. R. Santra, J. Zobeley, L. S. Cederbaum, N. Moiseyev, *Phys. Rev. Lett.* **85**, 4490 (2000).
2. T. Jahnke *et al.*, *Phys. Rev. Lett.* **93**, 163401 (2004).
3. T. Jahnke *et al.*, *J. Electron Spectrosc. Relat. Phenom.* **141**, 229 (2004).
4. R. Feifel, J. H. D. Eland, D. Edvardsson, *J. Chem. Phys.* **122**, 144308 (2005).
5. S. Hsieh, J. H. D. Eland, *J. Phys. At. Mol. Opt. Phys.* **29**, 5795 (1996).
6. S. D. Price, J. H. D. Eland, *J. Phys. At. Mol. Opt. Phys.* **24**, 4379 (1991).
7. L. Miaja-Avila *et al.*, *Phys. Rev. Lett.* **101**, 046101 (2008).
8. M. Drescher *et al.*, *Nature* **419**, 803 (2002).
9. B. Boudaiffa, P. Cloutier, D. Hunting, M. A. Huels, L. Sanche, *Science* **287**, 1658 (2000).
10. A. Kuleff, L. S. Cederbaum, *Phys. Rev. Lett.* **98**, 083201 (2007).
11. A. Rundquist *et al.*, *Science* **280**, 1412 (1998).
12. E. Gagnon *et al.*, *Science* **317**, 1374 (2007).
13. E. Gagnon *et al.*, *Rev. Sci. Instrum.* **79**, 063102 (2008).
14. J. Yang *et al.*, *J. Chem. Phys.* **128**, 091102 (2008).
15. A. Dreuw, L. S. Cederbaum, *Phys. Rev. A* **63**, 012501 (2000).
16. X.-B. Wang, L.-S. Wang, *Nature* **400**, 245 (1999).
17. H. Feshbach, *Ann. Phys.* **5**, 357 (1958).
18. C. A. Regal, C. Ticknor, J. L. Bohn, D. S. Jin, *Nature* **424**, 47 (2003).
19. S. Jochim *et al.*, *Science* **302**, 2101 (2003).
20. L. S. Cederbaum *et al.*, *J. Phys. B* **10**, L549 (1977).
21. M. Lundqvist, D. Edvardsson, P. Baltzer, M. Larsson, B. Wannberg, *J. Phys. At. Mol. Opt. Phys.* **29**, 499 (1996).
22. H. Lischka, R. Shepard, F. B. Brown, I. Shavitt, *Int. J. Quantum Chem. Symp.* **15**, 91 (1981).
23. R. Shepard *et al.*, *Int. J. Quantum Chem. Symp.* **22**, 149 (1988).
24. H. Lischka *et al.*, *Phys. Chem. Chem. Phys.* **3**, 664 (2001).
25. T. H. Dunning, *J. Chem. Phys.* **90**, 1007 (1989).
26. R. I. Hall, *et al.*, *Phys. Rev. Lett.* **68**, 2751 (1992).
27. Y. Hikosaka, *et al.*, *J. Chem. Phys.* **119**, 7693 (2003).
28. P. M. Dehmer, W. L. Luken, W. A. Chupka, *J. Chem. Phys.* **67**, 195 (1977).

29. We thank J. H. D. Eland and B. Krassig for helpful discussions. We acknowledge support for this work from NSF through the Physics Frontiers Centers Program and from the Office of Basic Energy Sciences, Office of Science, U.S. Department of Energy (DOE) (H.C.K. and M.M.M. under grant DOE DE-FG02-99ER14982; R.S. and P.H. under contract DE-AC02-06CH11357).

Supporting Online Material

www.sciencemag.org/cgi/content/full/322/5904/1081/DC1
SOM Text
Figs. S1 and S2
References

11 August 2008; accepted 15 October 2008
10.1126/science.1164498

Photosynthetic Control of Atmospheric Carbonyl Sulfide During the Growing Season

J. E. Campbell,[1]*† G. R. Carmichael,[2] T. Chai,[3] M. Mena-Carrasco,[4,5] Y. Tang,[2] D. R. Blake,[6] N. J. Blake,[6] S. A. Vay,[7] G. J. Collatz,[8] I. Baker,[9] J. A. Berry,[10] S. A. Montzka,[11] C. Sweeney,[12] J. L. Schnoor,[1] C. O. Stanier[2]

Climate models incorporate photosynthesis-climate feedbacks, yet we lack robust tools for large-scale assessments of these processes. Recent work suggests that carbonyl sulfide (COS), a trace gas consumed by plants, could provide a valuable constraint on photosynthesis. Here we analyze airborne observations of COS and carbon dioxide concentrations during the growing season over North America with a three-dimensional atmospheric transport model. We successfully modeled the persistent vertical drawdown of atmospheric COS using the quantitative relation between COS and photosynthesis that has been measured in plant chamber experiments. Furthermore, this drawdown is driven by plant uptake rather than other continental and oceanic fluxes in the model. These results provide quantitative evidence that COS gradients in the continental growing season may have broad use as a measurement-based photosynthesis tracer.

Parameterizations of carbon-climate feedbacks in climate models are based on climate sensitivities for photosynthesis and respiration that are highly uncertain (*1*–*3*). Measurement-based estimates of photosynthesis or respiration fluxes at large scales (>10^4 km^2) are needed to investigate these feedback mechanisms. Whereas photosynthesis and respiration-flux estimates have been made using eddy flux (*4*, *5*) and isotope techniques (*6*), robust tools for investigating these processes at large scales are currently lacking.

Recent work suggests potential for the use of atmospheric carbonyl sulfide (COS) as a photosynthesis tracer, on the basis of similarities observed between COS and CO_2 in a global air-monitoring network (*7*). The similarities are attributable to the simultaneous uptake of COS and CO_2 in photosynthetic gas exchange by terrestrial plants (*8*). COS has also been studied as a source of stratospheric aerosol (*9*, *10*), with recent reports suggesting that COS is a major source and that its contribution may be closely linked to continental surface fluxes (*11*, *12*).

Past models of COS plant uptake assume a 1:1 relation between relative uptake of COS and net primary productivity (NPP) (*13*–*16*). This relation was challenged by plant chamber (*8*) and atmospheric measurement studies (*7*), which suggest a new model of uptake that is related to photosynthesis [gross primary productivity (GPP)] and yields four to six times the uptake of the NPP-based models. COS uptake is related to GPP because atmospheric COS and CO_2 diffuse at similar rates into stomata, dissolve at similar rates into intercellular plant water, and are consumed by photosynthesis enzymes (*17*, *18*). COS is taken up preferentially to CO_2 because

[1]Department of Civil and Environmental Engineering, University of Iowa, Iowa City, IA 52242, USA. [2]Center for Global and Regional Environmental Research, University of Iowa, Iowa City, IA 52242, USA. [3]Science and Technology Corporation, Hampton, VA 23666, USA. [4]Department of Environmental Engineering, Universidad Andrés Bello, Santiago, Chile. [5]Molina Center for Energy and the Environment, Massachusetts Institute of Technology, Cambridge, MA 02139, USA. [6]Department of Chemistry, University of California, Irvine, CA 92697, USA. [7]NASA Langley Research Center, Hampton, VA 23681, USA. [8]Biospheric Sciences Branch, NASA-Goddard Space Flight Center, Greenbelt, MD 20771, USA. [9]Department of Atmospheric Science, Colorado State University, Fort Collins, CO 80523, USA. [10]Department of Global Ecology, Carnegie Institution of Washington, Stanford, CA 94305, USA. [11]Global Monitoring Division, National Oceanic and Atmospheric Administration (NOAA) Earth System Research Laboratory, Boulder, CO 80305, USA. [12]Cooperative Institute for Research in Environmental Sciences, University of Colorado, Boulder, CO 80304, USA.

*Present address: College of Engineering, University of California, Merced, CA 95344, USA.
†To whom correspondence should be addressed. E-mail: ecampbell3@ucmerced.edu

photosynthesis enzymes transform one-third of the dissolved CO_2 in leaf water but irreversibly transform most of the dissolved COS (*19*, *20*). The remainder of the dissolved CO_2 diffuses back to the atmosphere. The chamber studies suggest a GPP-based uptake model

$$F = GPP \cdot \frac{[COS]}{[CO_2]} \cdot V_{COS/CO_2} \qquad (1)$$

where F is COS plant uptake, GPP is the photosynthetic uptake of CO_2 by terrestrial plants, $[COS]/[CO_2]$ is the ratio of ambient concentrations, and V_{COS/CO_2} is the leaf-scale relative uptake measured during plant chamber experiments.

This GPP-based model was found in recent work to be qualitatively consistent with variations of global atmospheric measurements, suggesting that the total atmospheric lifetime of COS is only 1.5 to 3 years (*7*, *21*). However, it remains to be determined whether atmospheric COS measurements are quantitatively consistent with GPP-based plant uptake.

To provide a quantitative test of the relation between GPP and atmospheric COS, we compared atmospheric COS measurements from an airborne experiment with two simulations from a three-dimensional atmospheric transport model; one simulation was driven by the GPP-based uptake, and the second was driven by the NPP-based uptake. The airborne experiment, the Intercontinental Chemical Transport Experiment–North America (INTEX-NA), included 1741 daytime measurements of COS over continental North America between the surface and 12 km in altitude during July and August 2004. The experiment also included measurements of CO_2 (*22*) and many other species (*23*). We compared these INTEX-NA observations to the NOAA Earth System Research Laboratory (NOAA/ESRL) airborne observations made during July and August of 2005, 2006, and 2007 (*7*). To interpret the INTEX-NA observations, we simulated COS and CO_2 concentrations over North America for the INTEX-NA period (*24*, *25*). The COS simulations were driven by plant uptake, soil sinks, and ocean and anthropogenic sources (direct and indirect). We calculated GPP-based plant uptake (Eq. 1) by scaling regional GPP fluxes (*26*) by leaf-scale relative uptake estimates. The NPP-based uptake and other surface fluxes were taken from a recent inventory of gridded surface fluxes (*14*). We simulated CO_2 concentrations using ecosystem, ocean, and anthropogenic surface fluxes. See the supporting online material (SOM) for details on observations and model simulations.

The persistent vertical drawdown (Fig. 1) and variability (Fig. 2) in the boundary layer are well represented by the GPP model, whereas the NPP model performs poorly. Plant uptake was found to be dominant over other sources and sinks in the continental COS budget during the growing season (Fig. 3), a necessary condition for the use of COS as a photosynthesis tracer. These results are discussed below.

The mean modeled and measured CO_2 concentrations along the INTEX-NA flight paths (Fig. 1A) show the expected net uptake of CO_2 and boundary-layer mixing during the growing season (*27*). The agreement between the observed and modeled drawdown indicates that atmospheric mixing is well represented in the model. Whereas model underestimation in the 2- to 5-km altitude range may suggest some deficiencies in the simulated mixing, there is only a 10% difference between the observed and modeled estimates of the column-integrated drawdown (*21*).

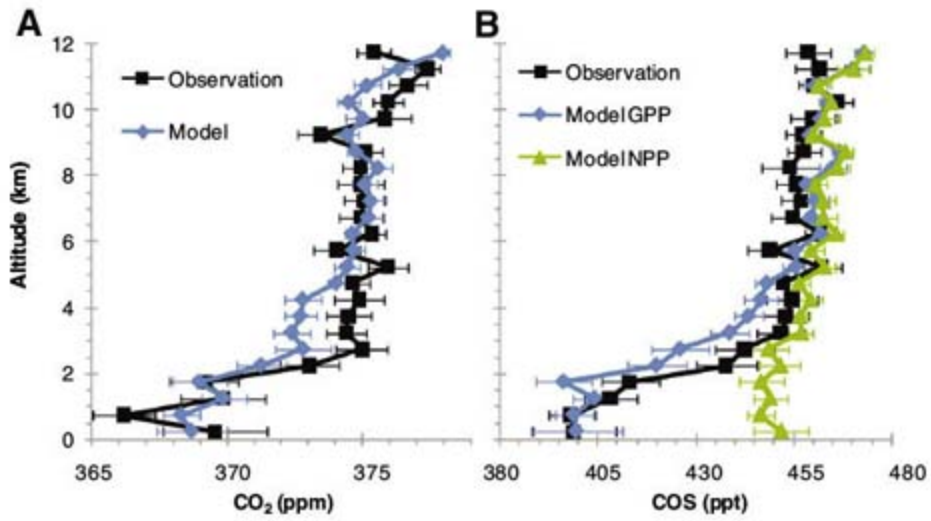

Fig. 1. Vertical profiles of COS and CO_2 along INTEX-NA flight paths. Mean concentrations for all continental INTEX-NA data for CO_2 (**A**) and COS (**B**) (error bars indicate ± 95% CI, n = 70 average observations in each bin). Model results were interpolated to time and location of each observation. ppm, parts per million.

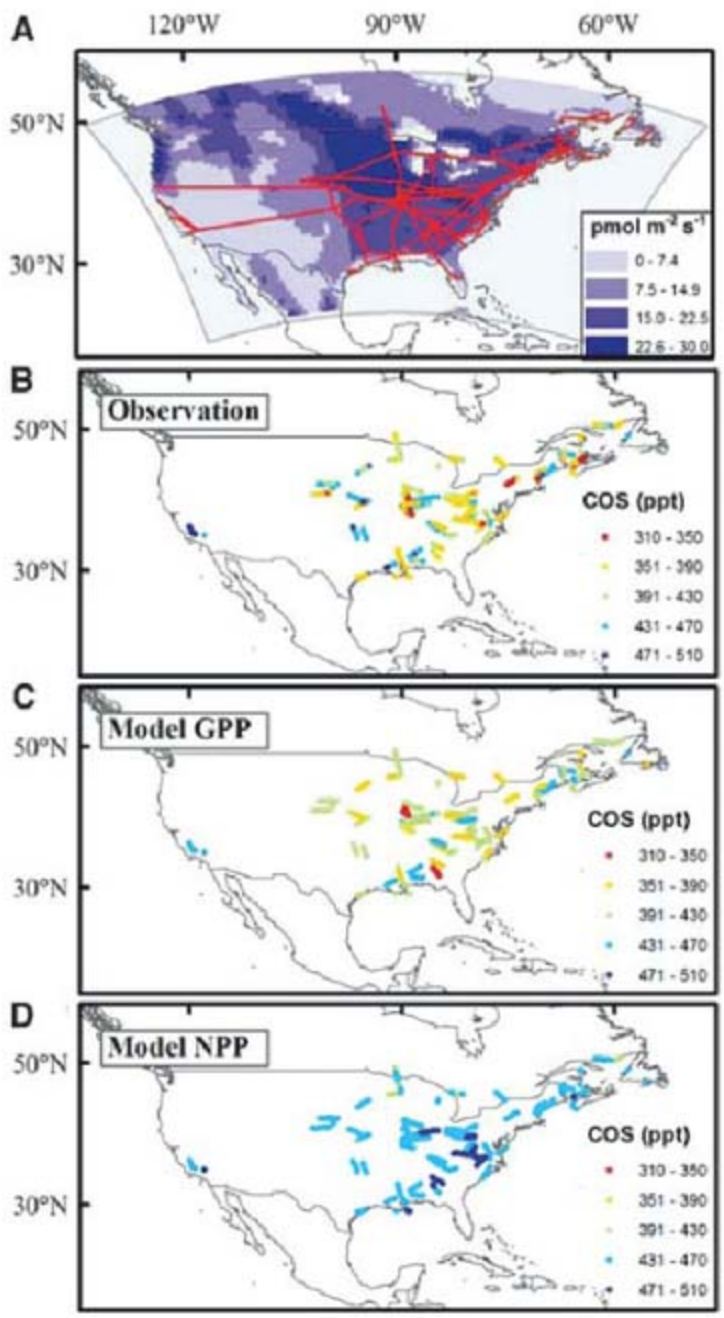

Fig. 2. COS plant uptake flux and boundary-layer concentrations. (**A**) COS plant uptake flux (mean July 2004) calculated by scaling modeled GPP by leaf-relative uptake. See SOM for details. Continental INTEX-NA DC8 flight paths (red lines) are shown within the model domain (gray box). (**B** to **D**) Modeled and observed atmospheric COS concentrations at all continental sampling points under 2 km in altitude above sea level (ASL).

The mean COS vertical profile (from the 1741 INTEX-NA samples) also shows considerable drawdown in the boundary layer (Fig. 1B). The INTEX-NA concentration drawdown (difference between 6 to 8 km and 0 to 2 km in altitude) of 59.9 ± 8.9 parts per thousand (ppt) [mean ± 95% confidence interval (CI), n = 50 vertical profiles] for sampling in July and August of 2004 is consistent with the NOAA/ESRL drawdown of 55.9 ± 19.0 ppt (mean ± 95% CI, n = 12 airborne sites) for sampling in July and August of 2005 through 2007. The NPP model largely underestimates the observed drawdown as expected (*13*, *16*), whereas the GPP model has good agreement with the observed drawdown. As with CO_2, some deficiencies in the GPP model are apparent in the 2- to 5-km altitude range. However, there is only a 15% difference between the observed and GPP model estimates of the column-integrated drawdown (*21*). The column-integrated drawdown for the observed data was 4.2 times the NPP model estimate (*21*). Sensitivity analysis showed that the drawdown estimates are robust with respect to boundary condition uncertainty (*21*).

Maps of INTEX-NA boundary-layer COS concentrations show considerable variability in the boundary-layer observations (SD = 39 ppt), and this variability is similar to that in the GPP model (SD = 34 ppt) but much larger than that in the NPP model (SD = 24 ppt) (Fig. 2). The GPP model captures much of the observed variability in the boundary-layer COS concentrations with a correlation coefficient of 0.71 (n = 440). This GPP model performance is similar to the a priori performance in CO_2 studies that use a model-observations analysis to infer surface-flux estimates (*28*). The variability in the GPP model is largely driven by the magnitude of the plant uptake and caused by the mixing of background air with boundary-layer air that is depleted of COS (*21*).

The combined evidence from the concentration drawdown, column-integrated drawdown, boundary-layer variation, CO_2 profiles, and NOAA/ESRL data are consistent with the GPP-based model rather than the NPP-based model. Next, we consider the relative influence of the different surface fluxes on the COS airborne samples using transport simulations driven by only one surface flux at a time (Fig. 3A). Anthropogenic COS emissions (direct and indirect) are concentrated in the eastern United States but result in a boundary-layer enhancement that is less than one-third of the vegetative drawdown (*21*). The COS soil up-

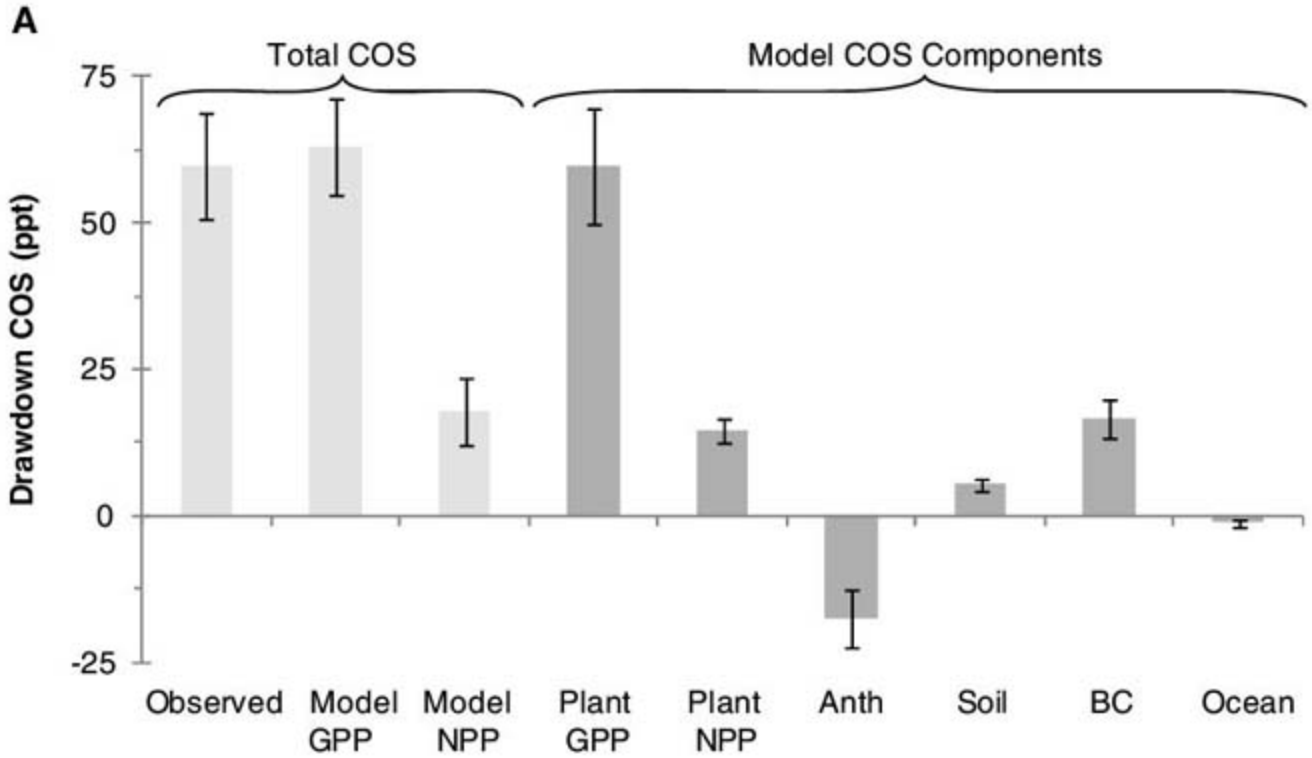

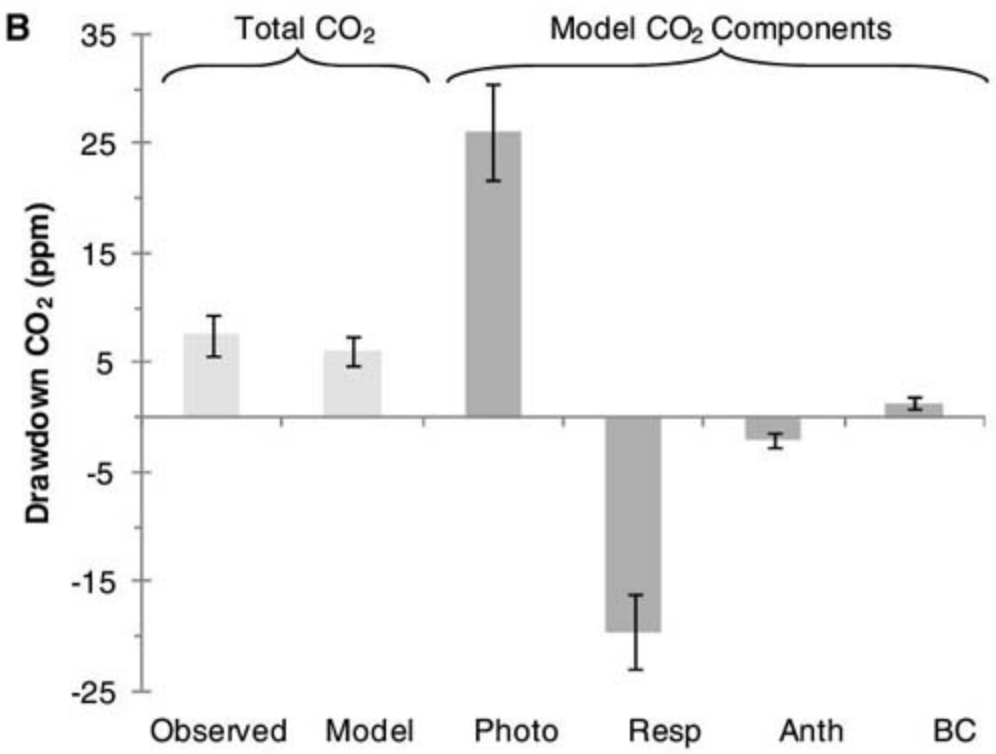

Fig. 3. Tropospheric drawdown for observed and modeled concentrations along continental INTEX-NA flight paths. Tropospheric drawdown of COS (**A**) and CO_2 (**B**), for total (left bracket) and modeled components (right bracket) as the difference between mean 6- to 8-km and 0- to 2-km altitude ASL concentrations for all continental INTEX-NA data (error bars indicate ± 95% CI, n = 50 vertical profiles). Anth, anthropogenic; Photo, photosynthesis; Resp, ecosystem respiration; BC, boundary condition. Positive drawdown is removal from the atmosphere, and negative drawdown is a source to the atmosphere. Individual component drawdowns (right bracket) are based on multiple atmospheric transport model simulations using only one flux at a time as input and fixed boundary conditions.

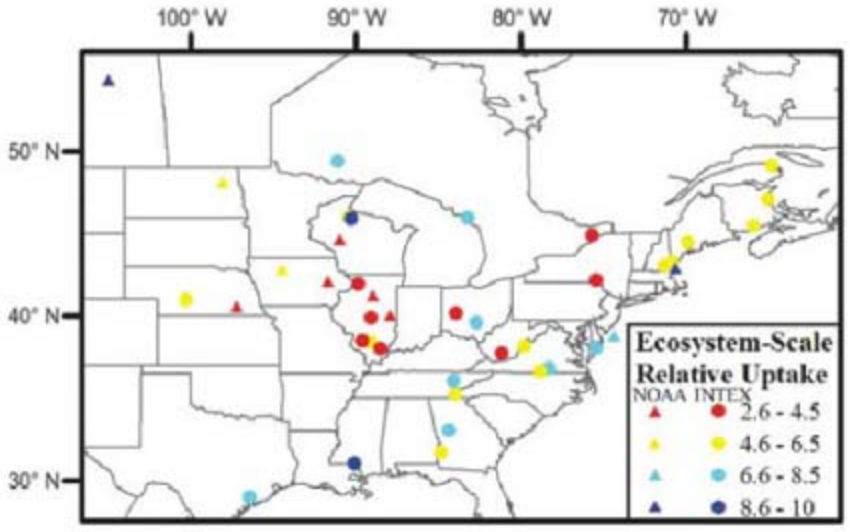

Fig. 4. Observed ERU of COS to CO_2 from INTEX-NA and NOAA/ESRL measurements. ERU is the normalized drawdown of COS relative to the normalized drawdown of CO_2, calculated from the difference between airborne observations in the 0- to 2-km and 6- to 8-km altitude bins. Samples were taken in July and August 2004 for INTEX-NA (circles) and July and August of 2005 through 2007 for NOAA/ESRL (triangles). Repeated vertical profiles at the same location are shown as a single average. (See SOM for details.)

take is <10% of the plant uptake, which is consistent with available field observations (*29*). Although ocean fluxes are a large source globally (*14*), they have only a small influence on the vertical profile for the continental growing season. There may be large missing sources in the global COS budget that could be important in relation to plant uptake for some regions (*8*). However, the good agreement of modeled and observed COS during INTEX-NA suggests that these missing sources are not located in North America during the growing season. Whereas the COS drawdown is dominated by plant uptake, the CO_2 drawdown has offsetting influences of photosynthesis and respiration components that are many times the net CO_2 drawdown (Fig. 3B). These offsetting components make it challenging to apply CO_2 measurements to separately investigate photosynthesis and respiration, reinforcing the need for a tracer such as COS.

This evidence that continental-scale variations of atmospheric COS over North America are driven by the COS/photosynthesis relation suggests the potential use of COS as a carbon-cycle tracer. One tracer application is to estimate the ratio of GPP CO_2 fluxes relative to net ecosystem exchange (NEE) CO_2 fluxes using relations between simultaneous observations of COS and CO_2. For vertical profile observations, a useful relation is the ecosystem-scale relative uptake (ERU), which is the ratio of the relative drawdown of COS to CO_2 (*7*, *21*). When plant uptake is the dominant flux, the ERU is proportional to the ratio of GPP/NEE with a proportionality constant that is the leaf-scale relative uptake. The INTEX-NA and NOAA/ESRL observations have a mean ERU of 5.7 ± 0.6 (mean ± SD, n = 31 vertical profiles, July and August 2004) and 5.7 ± 2.1 (mean ± SD, n = 10 airborne sites, July and August of 2005 through 2007), respectively. For a mean continental leaf-scale relative uptake of 2.2 (*21*), these ERU values imply a GPP/NEE ratio of 2.6, which is similar to estimates of GPP/NEE of crops during mid–growing season from eddy-flux studies (*5*, *7*, *30*). Both INTEX-NA and NOAA/ESRL observations show lower ERU values over the mid-continent where C4 corn is extensive (Fig. 4). This regional depression in ERU could reflect a decrease in the ratio of GPP/NEE for C4 corn plants that has also been observed in eddy covariance studies of the North American growing season (*5*). Alternatively, lower leaf-scale relative uptake values have been hypothesized for C4 plants (*7*, *8*) and we suggest that the leaf-scale relative uptake and the ratio of GPP/NEE for C4 plants be explored more widely. Although the ERU could also be influenced by a regional anthropogenic COS source, the anthropogenic source relative to the plant uptake is rather weak in this region (*21*).

Another tracer application is to estimate the photosynthesis CO_2 flux with the use of an inverse analysis (*31*) of the COS model concentration error. Inverse analyses must consider multiple sources of model error, including transport parameterizations, different surface fluxes, boundary conditions, and representation error. For the COS inversion, the two flux parameters, other than GPP (Eq. 1), must be well constrained, and the COS fluxes other than plant uptake must be well known or relatively small, as may be the case for the continental growing season. One flux parameter, the concentration ratio parameter (Eq. 1), is well constrained by observations and has an observed variability of <10% in the INTEX-NA boundary-layer samples (n = 440). The other flux parameter, leaf-scale relative uptake, may be more uncertain because of the dependence on plant type and growth conditions, but the success of the simple leaf-scale uptake mapping used in this work is promising (*21*). Knowledge of leaf-scale uptake could be improved with additional plant chamber and ambient studies in support of efforts to recover GPP values.

The results presented here suggest global COS plant uptake and vertical gradients that are more than four times those predicted in previous global models (*14*–*16*). This finding implies a large missing source in the global COS budget (*7*, *8*) and large uncertainty in how previous global models have predicted the transfer of COS to the stratosphere. Applications of the GPP model at a global scale should help to resolve uncertainties in COS budgets and could improve our understanding of the relation between COS surface fluxes and stratospheric aerosol. However, the most intriguing application may be to recover GPP and ecosystem respiration information by inverse analysis of atmospheric COS measurements.

References and Notes

1. P. M. Cox, R. A. Betts, C. D. Jones, S. A. Spall, I. J. Totterdell, *Nature* **408**, 184 (2000).
2. C. B. Field, D. B. Lobell, H. A. Peters, N. R. Chiariello, *Annu. Rev. Environ. Resour.* **32**, 1 (2007).
3. P. Friedlingstein *et al.*, *J. Clim.* **19**, 3337 (2006).
4. P. Ciais *et al.*, *Nature* **437**, 529 (2005).
5. E. Falge *et al.*, *Agric. For. Meteorol.* **113**, 53 (2002).
6. D. R. Bowling, P. P. Tans, R. K. Monson, *Global Change Biol.* **7**, 127 (2001).
7. S. A. Montzka *et al.*, *J. Geophys. Res.* **112**, D09302 (2007).
8. L. Sandoval-Soto *et al.*, *Biogeosciences* **2**, 125 (2005).
9. M. Chin, D. D. Davis, *J. Geophys. Res.* **100**, 8993 (1995).
10. P. J. Crutzen, *Geophys. Res. Lett.* **3**, 73 (1976).
11. J. Notholt *et al.*, in *SPARC Assessment of Stratospheric Aerosol Properties (ASAP)*, L. Thomason, T. Peter, Eds. (World Meteorological Organization World Climate Research Programme, Toronto, 2006), pp. 29–76.
12. J. Notholt *et al.*, *Science* **300**, 307 (2003).
13. N. J. Blake *et al.*, *J. Geophys. Res.* **113**, D09590 (2008).
14. A. J. Kettle, U. Kuhn, M. von Hobe, J. Kesselmeier, M. O. Andreae, *J. Geophys. Res.* **107**, 4658 (2002).
15. A. J. Kettle *et al.*, *Atmos. Chem. Phys.* **2**, 343 (2002).
16. E. Kjellström, *J. Atmos. Chem.* **29**, 151 (1998).
17. G. Protoschill-Krebs, J. Kesselmeier, *Bot. Acta* **105**, 206 (1992).
18. G. Protoschill-Krebs, C. Wilhelm, J. Kesselmeier, *Atmos. Environ.* **30**, 3151 (1996).
19. G. D. Farquhar *et al.*, *Nature* **363**, 439 (1993).
20. R. J. Francey, P. P. Tans, *Nature* **327**, 495 (1987).
21. Materials and methods are available as supporting material on *Science* Online.
22. Y. H. Choi *et al.*, *J. Geophys. Res.* **113**, D07301 (2008).
23. H. B. Singh, W. H. Brune, J. H. Crawford, D. J. Jacob, P. B. Russell, *J. Geophys. Res.* **111**, D24S01 (2006).
24. J. E. Campbell *et al.*, *Tellus B* **59B**, 199 (2007).
25. G. R. Carmichael *et al.*, *J. Geophys. Res.* **108**, 8823 (2003).
26. S. C. Olsen, J. T. Randerson, *J. Geophys. Res.* **109**, D02301 (2004).
27. C. Gerbig *et al.*, *J. Geophys. Res.* **108**, 4757 (2003).
28. D. M. Matross *et al.*, *Tellus B Chem. Phys. Meterol.* **58**, 344 (2006).
29. M. Steinbacher, H. G. Bingemer, U. Schmidt, *Atmos. Environ.* **38**, 6043 (2004).
30. A. E. Suyker, S. B. Verma, G. G. Burba, T. J. Arkebauer, *Agric. For. Meteorol.* **131**, 180 (2005).
31. C. D. Rodgers, *Inverse Methods for Atmospheric Sounding: Theory and Practice* (World Scientific, Singapore, 2000), p. 238.

32. We thank J. Kettle for COS flux data and C. Tebaldi, J. Dungan, T. Campbell, and D. Campbell for critical comments on the manuscript. This research was supported by a NASA Earth System Science Graduate Fellowship, Center for Global and Regional Environmental Research, NOAA Office of Oceanic and Atmospheric Research contribution to the North American Carbon Program, NASA INTEX, and NSF Information Technology Research grants. NOAA observations of COS and CO_2 were made possible by the assistance of P. Tans, C. Sweeney, L. Miller, T. Conway, P. Lang, C. Siso, and B. Hall.

Supporting Online Material

www.sciencemag.org/cgi/content/full/322/5904/1085/DC1

Materials and Methods
SOM Text
Figs. S1 to S5
Tables S1 to S3
References

31 July 2008; accepted 17 October 2008
10.1126/science.1164015

A Female *Homo erectus* Pelvis from Gona, Ethiopia

Scott W. Simpson,[1,2] Jay Quade,[3] Naomi E. Levin,[4,5] Robert Butler,[6] Guillaume Dupont-Nivet,[7] Melanie Everett,[8,9,10] Sileshi Semaw[9,10]*

Analyses of the KNM-WT 15000 *Homo erectus* juvenile male partial skeleton from Kenya concluded that this species had a tall thin body shape due to specialized locomotor and climatic adaptations. Moreover, it was concluded that *H. erectus* pelves were obstetrically restricted to birthing a small-brained altricial neonate. Here we describe a nearly complete early Pleistocene adult female *H. erectus* pelvis from the Busidima Formation of Gona, Afar, Ethiopia. This obstetrically capacious pelvis demonstrates that pelvic shape in *H. erectus* was evolving in response to increasing fetal brain size. This pelvis indicates that neither adaptations to tropical environments nor endurance running were primary selective factors in determining pelvis morphology in *H. erectus* during the early Pleistocene.

The modern human pelvis is uniquely modified to accommodate both bipedal locomotion and the birthing of large-brained offspring (*1*, *2*). The earliest known fossil hominid adult pelves are from small-bodied females (such as the 3.2-million-year-old *Australopithecus afarensis* specimen A.L. 288-1an/ao and the ~2.5- to 2.8-million-year-old *Au. africanus* specimen Sts14) that show anatomical adaptations to bipedal locomotion yet lack obstetric specializations. By the early Pleistocene, *Homo erectus* exhibited an absolute and relative increase in brain size, suggesting that the parturition of a large-brained fetus may have imposed novel selection on its pelvis. Few early *Homo* fossil pelvis fragments exist (*3*), and it is the 1.53-million-year-old juvenile male skeleton (KNM-WT 15000) from Kenya that has been central in assessing *H. erectus* pelvic morphology and body shape (*4*). The transversely narrow pelvis and torso reconstructed for this individual were suggested to be adaptations that enhanced locomotor effectiveness and thermoregulatory homeostasis in more open, semi-arid tropical environments (*4*, *5*). Estimates of female birth canal dimensions based on this fossil have been interpreted to suggest that *H. erectus* lacked derived obstetric modifications in the pelvis and that its small birth canal limited neonatal brain size (*3*, *6*) to a maximum of ~230 ml. This, in turn, was argued to have resulted in the birth of developmentally immature offspring that experienced rapid postnatal brain growth requiring a modern human–like degree of maternal investment and child-rearing behaviors (*6*).

Here we describe a nearly complete early Pleistocene adult female *H. erectus* pelvis and last lumbar vertebra (BSN49/P27a-d) from the upper Busidima Formation (*7*, *8*), dated 1.8 to <0.16 million years ago (Ma), in the Gona Paleoanthropological Research Project study area in the Afar Regional State, Ethiopia (Fig. 1). The BSN49 site is stratigraphically located between the Silbo Tuff (0.751 ± 0.022 Ma) and the base of the C1r polarity chron (1.778 Ma) (fig. S1). Consideration of the range of observed sediment accumulation rates in the Busidima Formation narrows the likely age of the fossil to 0.9 to 1.4 Ma (*8*). To date, *H. erectus* is the only hominid known from the early Pleistocene deposits in the Afar Depression. Early Acheulean artifacts are common at the BSN49 stratigraphic level. Analyses of carbon and oxygen stable isotopes from pedogenic carbonates and herbivore enamel from the BSN49 level indicate a semi-arid environment with a landscape dominated by C4 grasses and grazing herbivores (*8*).

The pelvis (Fig. 2) includes the sacrum and both os coxae with the first complete pubis from the early Pleistocene. Most of its distortion was produced by in situ fracture and carbonate cementation of the displaced fragments. The complete pelvis was reconstructed from high-resolution plaster casts. Despite minor residual asymmetry, the major functionally relevant dimensions and articular surfaces required little or no reconstruction and can be considered reliable for anatomical interpretation and mensuration (*8*).

The adult BSN49/P27 pelvis is transversely broad with laterally flaring ilia and anteriorly positioned acetabulocristal buttresses, long pubic rami, and a wide sciatic notch, which are all plesiomorphic characters shared with the australopithecines, other early (*3*) and middle (*9*, *10*) Pleistocene *Homo*, and Neandertals (*11*). The fossils attributable to *H. erectus* or early *Homo* [including KNM-WT 15000, KNM-ER 1808,

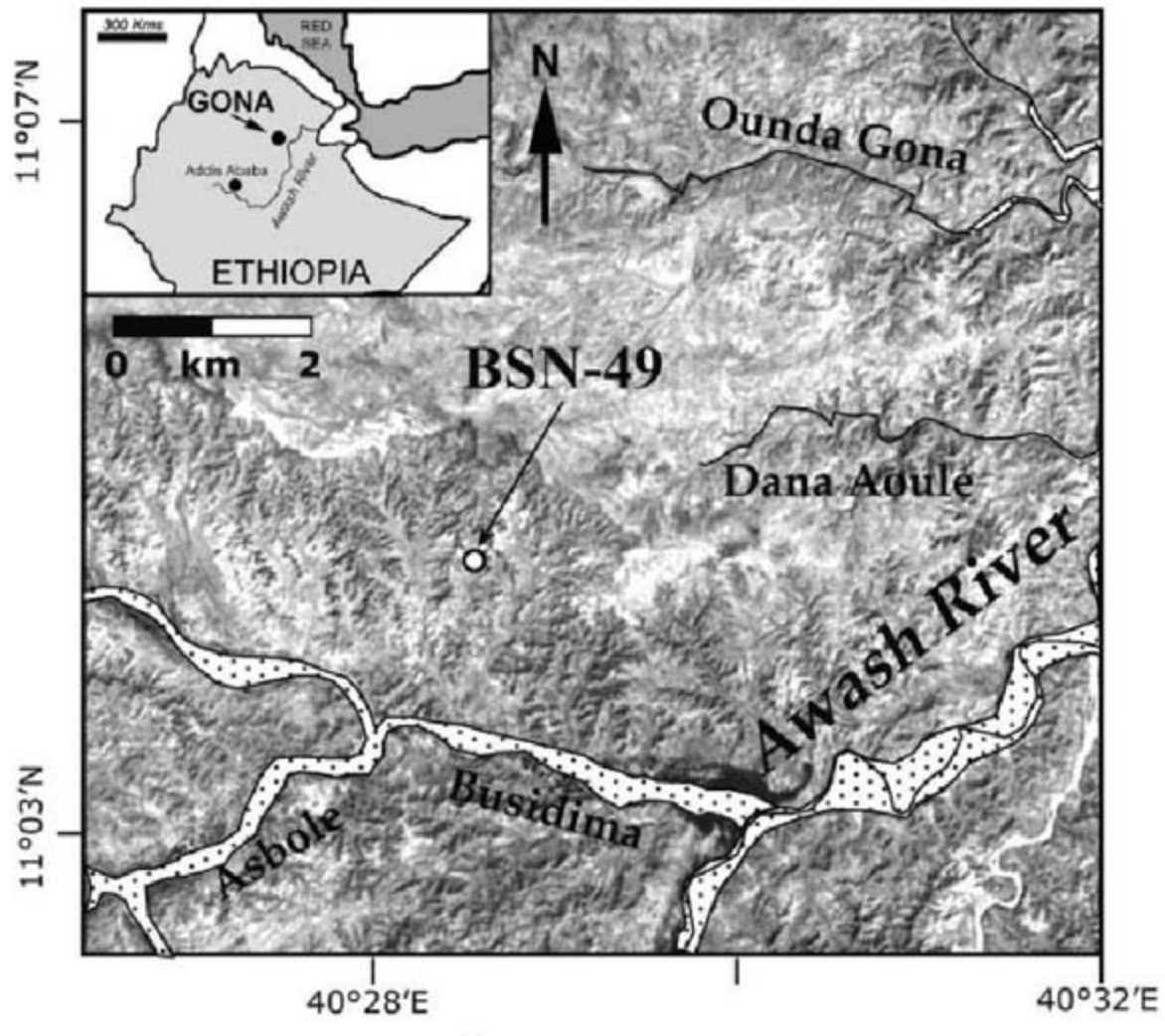

Fig. 1. Location of site BSN49. See (*8*) for additional information on site stratigraphy and tuff geochemistry.

[1]Department of Anatomy, Case Western Reserve University School of Medicine, Cleveland, OH 44106–4930, USA. [2]Laboratory of Physical Anthropology, Cleveland Museum of Natural History, Cleveland, OH 44106, USA. [3]Department of Geosciences/Desert Laboratory, University of Arizona, Tucson, AZ 85721, USA. [4]Department of Geology and Geophysics, University of Utah, Salt Lake City, UT 84112, USA. [5]Division of Geological and Planetary Sciences, California Institute of Technology, MC 100-23, Pasadena, CA 91125, USA. [6]Department of Physics, University of Portland, Portland, OR 97203–5798, USA. [7]Faculty of Geosciences, Utrecht University, Budapestlaan 17, 3584 CD Utrecht, Netherlands. [8]Department of Geological Sciences, Indiana University, Bloomington, IN 47407, USA. [9]The Stone Age Institute, 1392 West Dittemore Road, Gosport, IN 47433, USA. [10]Center for Research into the Anthropological Foundations of Technology (CRAFT), Indiana University, Bloomington, IN 47405, USA.

*To whom correspondence should be addressed. E-mail: ssemaw@indiana.edu

KNM-ER 3228, OH28, and UA-173/404+UA-466 (*3*, *12*)] span the early Pleistocene in Africa and exhibit laterally flaring ilia, wide (in terms of modern males) greater sciatic notches, tall thin pubic symphyseal faces, small auricular surfaces, and anteriorly placed iliac pillars. Except for overall size, the BSN49/P27 specimen is anatomically similar to these pelvis fossils (*8*). The BSN49/P27 pelvis shares with *Homo* such diagnostic characters (*8*) as an anteroposteriorly broadened birth canal, a thickened acetabulocristal buttress (iliac pillar), a sigmoid-shaped anterior inferior iliac spine, a shelf formed by attachment of the reflected head of the rectus femoris muscle, deepened fossa for the gluteus medius muscle, an increased height of the posterior ilium with an expanded retroauricular area, and angular elevation and anterior projection of the superior pubic rami (*13*). As in other *Homo* sacra, the BSN49/P27 alae are anteroposteriorly broad with marked periauricular excavation and a robust and projecting sacral tuberosity indicating a well-developed interosseous sacroiliac ligament complex: features that readily distinguish *Homo* from the australopithecines (*8*).

The BSN49/P27 acetabulae are small, with an estimated femoral head diameter of 33.4 to 36.8 mm (*8*)—substantially smaller than the femoral head of other early Pleistocene specimens [such as KNM-WT 15000: 44.9 mm (*14*)]. Regressions estimating femur length and stature based on the major load-bearing articular surfaces of the pelvis (*8*) predict a stature for the BSN49/P27 individual of 1.20 to 1.46 m, markedly shorter than the 1.85 m adult stature estimated for the male KNM-WT 15000 individual (*4*). Although *H. erectus* is widely characterized as apomorphically exhibiting an increase in stature and reduction in stature dimorphism, the data supporting this idea are surprisingly meager. With the recent discovery of *H. erectus* crania and postcrania from smaller individuals [such as KNM-OL 45500 (*15*), KNM-ER 42700 (*16*), and Dmanisi (*17*, *18*)], it is apparent that body size range in *H. erectus* has been underestimated, and a size "Rubicon" should not be part of the species diagnosis (*16*). The presence of very wide greater sciatic notches (*8*) and subpubic angle (table S5), everted ischia, rectangular pubic bodies with a ventral arc, a subpubic concavity, a large sacral angle (*19*), a nonprojecting sacral promontory, a symmetrically oval pelvic inlet, and a preauricular sulcus are all traits diagnostic of a female pelvis. Thus, the BSN49/P27 pelvis is from a short-statured *H. erectus* adult female.

The BSN49/P27 pelvis is obstetrically capacious for such a short-statured individual. The fossil's inlet circumference is within modern female ranges (*8*). The obstetrically important bispinous (pelvic midplane) and bituberular (pelvic outlet) transverse breadths of BSN49/P27 are greater than in most modern females (Fig. 3) (*8*). Size-normalized comparisons and multivariate analyses of the pelvic inlet and midplane demonstrate the obstetrically derived shape of the BSN49/P27 birth canal (Fig. 3, C and D) (*8*).

Humans are unusual among the hominoids in having a near identity in size between the neonatal head and the birth canal dimensions that places both mother and neonate at substantial risk of a traumatic birth. When these anatomical relationships in humans were used to estimate neonatal head size in *H. erectus*, it was seen that the BSN49/P27 pelvis was capable of birthing an offspring with estimated maximal brain volume of up to 315 ml (*8*)—over 30% greater than previously predicted from the KNM-WT 15000 pelvis (*6*), although this value is similar to growth-based estimates (*20*). Neonatal brain size was approximately 30 to 50% (the mean ratio is 34 to 36%) of early Pleistocene *H. erectus* adult brain size [~600 to 1067 ml (mean = 880 ml, n = 18 crania)] (*21*), an intermediate value between that of chimpanzees (~40%) and modern humans (~28%) (*20*). This new estimate of *H. erectus* neonatal brain size, in tandem with the revised age at death (~0.5 to 1.5 years) of the child's cranium from Perning (Mojokerto), Indonesia (<1.81 Ma) (*22*), suggests that *H. erectus* had a prenatal brain growth rate similar to that of humans but a postnatal brain and somatic growth rate intermediate between that of chimpanzees and humans (*23*).

The enlarged neonatal brain in *H. erectus* required a concomitant increase in the dimensions of their bony birth canal. Two nonexclusive means of enlarging birth canal size beyond the primitive *Australopithecus* condition (*1*) are an increase in female body size [larger females can have isometrically larger pelves (*24*)] or developmentally mediated changes in pelvic shape resulting in pelvic sexual dimorphism. Given this individual's short stature with a capacious birth canal and characteristically female pelvic shape,

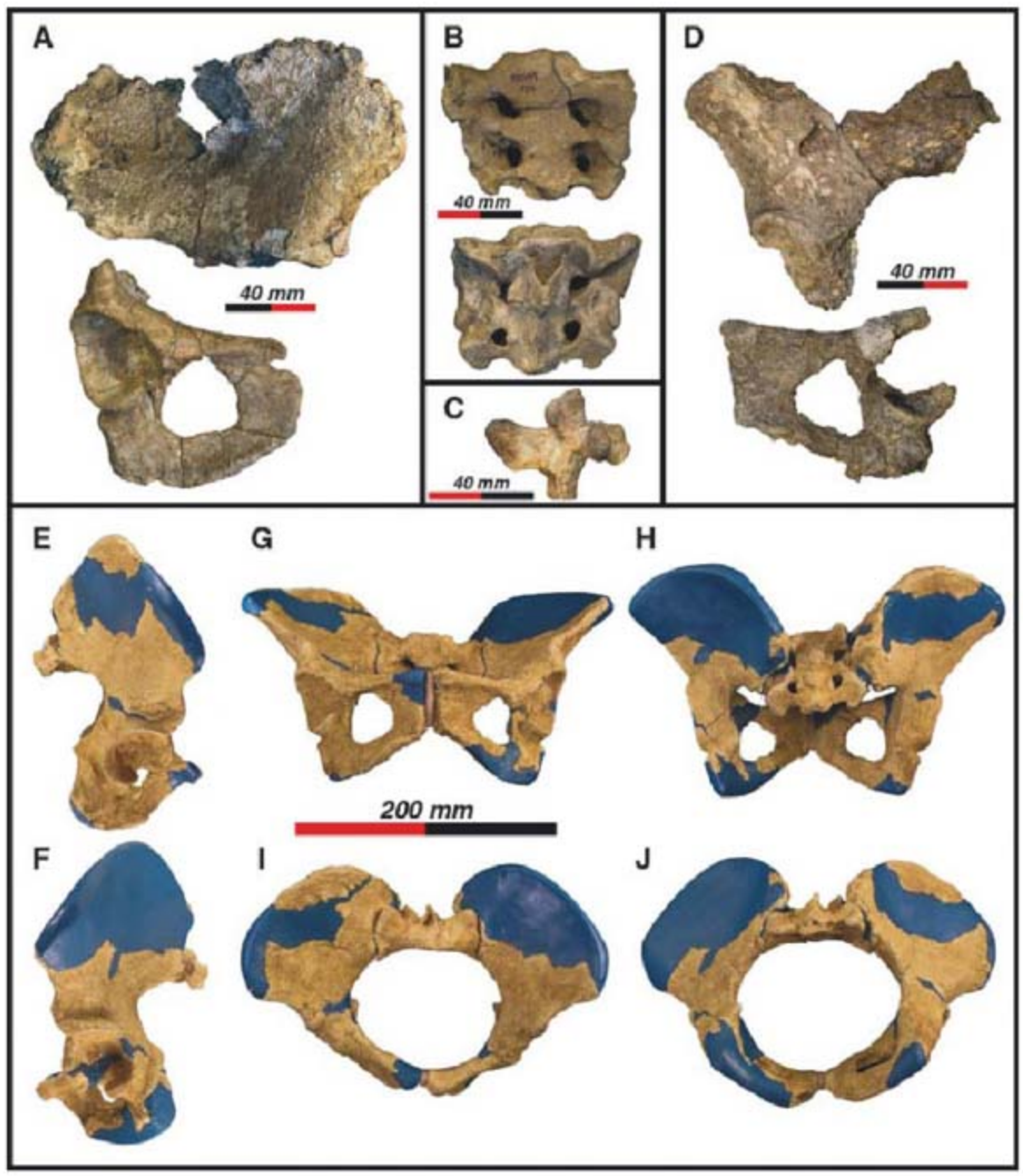

Fig. 2. Illustrations of major elements of the BSN49/P27 pelvis and lumbar vertebra and reconstruction of the pelvis. (**A**) Right os coxa with posterolateral view of the ilium and anterolateral view of an ischiopubic fragment. (**B**) Anterior and posterior views of the sacrum. (**C**) Right lateral view of the lumbar vertebra. (**D**) Posterolateral view of the left ilium and anterolateral view of the left ischiopubic fragment. (**E**) Right lateral view. (**F**) Left lateral view. (**G**) Anterior view. (**H**) Posterior view. (**I**) Pelvic inlet. (**J**) Pelvic outlet. The blue portions of the cast indicate areas that have been reconstructed or restored. Scale bar for (A) to (D), 40 mm; scale bar for (E) to (J), 200 mm.

it is clear that the latter applies. This resulted in a recognizably dimorphic pelvis by the early Pleistocene, with females demonstrating the distinctive obstetric anatomy required to deliver a large-brained offspring. This derived anatomy indicates that the fetal cephalic–maternal pelvic disproportion, which directly affects reproductive success, was a significant selective factor on female pelvic morphology at that time.

This individual's absolutely wide bi-iliac breadth (288 mm) is greater than the mean width of modern females and males from eight diverse populations (*8*, *19*, *25*, *26*), indicating that the BSN49/P27 individual had a very broad trunk. Its bi-iliac breadth is exceeded in the fossil record only by the very large middle and late Pleistocene pelves from Atapuerca, Spain (*9*), Jinniushan, China (*10*), and Kebara, Israel (*11*), which are specimens that retain the primitive condition of laterally flaring ilia. The only ancient pelvis that does not exhibit marked lateral flare is the reconstructed KNM-WT 15000 pelvis, a reconstruction that has been questioned (*3*, *9*).

Many anatomical changes in the human pelvis have occurred since the middle Pleistocene, including a narrowing of the interacetabular distance; an increase in the anteroposterior breadth of the birth canal, with shorter, elevated pubic rami; and a decrease in the degree of iliac flaring, leading to a reduction of the bi-iliac breadth (*13*). Some authors have suggested that these anatomical adaptations had their roots in the early Pleistocene as a locomotor adaptation by *H. erectus* to endurance running (*5*). The BSN49/P27 pelvis does not exhibit any of these anatomical modifications or others proposed to be adaptive responses to this behavior, such as tall stature, enlarged acetabulae, or a narrow torso. Clearly, improving locomotor effectiveness, as exhibited by a relative and absolute increase in lower limb length, was a component of the early *Homo* adaptive complex. However, the earliest fossil evidence of the modern human pelvis is documented about 100,000 years ago from Skhul, Israel, indicating both the recency of this morphology and the historical stability of the plesiomorphic transversely broad pelvis.

Modern humans display a relation between body shape and ambient temperature and humidity, with individuals living in more temperate and Arctic climates having absolutely and relatively broader torsos, and peoples in tropical arid/semi-arid areas possessing narrower trunks (*27*). The BSN49/P27 pelvis represents a short-statured, broad-hipped individual who would have had an extreme bi-iliac breadth/stature ratio characteristic of more temperate-adapted modern humans and not the tall narrow body form previously identified in *H. erectus* as an adaptation to tropical semi-arid environments (*4*, *8*). Thus, although early *Homo* lived in a diversity of environments, because of their unique pelvic shape they did not exhibit the same ecogeographic patterns of body form as seen in modern humans (*10*).

The first *H. erectus* fossils were found over 100 years ago. Additional *H. erectus* remains have since been recovered from numerous sites spanning over a million years, thousands of miles, and a wide diversity of ecological zones. These fossils have documented a substantial increase in endocranial capacity in *H. erectus* over their Pliocene ancestors. Despite this rich history, few complete fossil postcrania (*18*) have been recovered, and basic features of *H. erectus* body shape remain poorly understood. The transversely broad torso, clearly evident in this short individual, requires reappraisal of some current models of locomotor and ecogeographic adaptations in African early Pleistocene *H. erectus*. It is now clear that the *H. erectus* pelvis retained many elements of its australopithecine heritage, although substantially modified by the demands of birthing large-brained offspring.

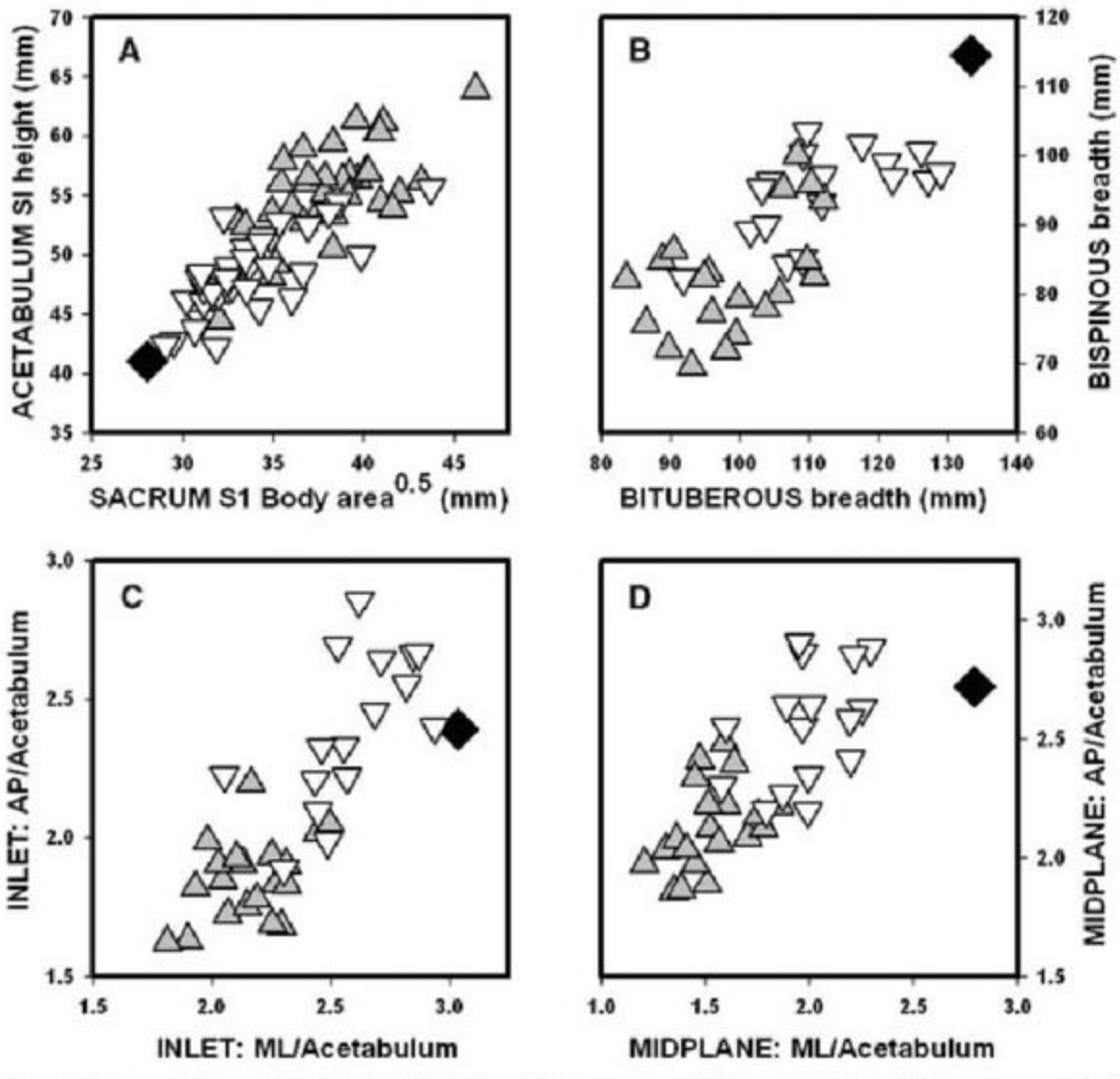

Fig. 3. Comparative pelvimetrics. (**A**) Plot of acetabulum superoinferior diameter with the square root of the sacral S1 body area (*8*). (**B**) Plot of bituberous breadth (pelvic outlet breadth) and bispinous breadth (pelvic midplane breadth). (**C**) Anteroposterior (AP) and mediolateral (ML) birth canal inlet dimensions normalized by acetabulum superoinferior diameter. (**D**) Anteroposterior and transverse birth canal midplane dimensions normalized by acetabulum superoinferior diameter. Human data are from The Hamann-Todd collection, Cleveland Museum of Natural History, Cleveland, Ohio. Open inverted triangles, females; gray triangles, males; black diamond, BSN49/P27.

References and Notes

1. C. O. Lovejoy, K. G. Heiple, A. H. Burstein, *Am. J. Phys. Anthropol.* **38**, 757 (1973).
2. R. G. Tague, C. O. Lovejoy, *J. Hum. Evol.* **35**, 75 (1998).
3. C. B. Ruff, *Am. J. Phys. Anthropol.* **98**, 527 (1995).
4. C. B. Ruff, A. Walker, in *The Nariokotome* Homo erectus *Skeleton*, A. Walker, R. Leakey, Eds. (Harvard Univ. Press, Cambridge, MA, 1993), pp. 234–265.
5. D. M. Bramble, D. E. Lieberman, *Nature* **432**, 345 (2004).
6. A. Walker, C. B. Ruff, in *The Nariokotome* Homo erectus *Skeleton*, A. Walker, R. Leakey, Eds. (Harvard Univ. Press, Cambridge, MA, 1993), pp. 221–233.
7. J. Quade *et al.*, *Geol. Soc. Am. Bull.* **116**, 1529 (2004).
8. Materials and methods are available as supporting material on *Science* Online.
9. J.-L. Arsuaga *et al.*, *Nature* **399**, 255 (1999).
10. K. Rosenberg, Z. Lü, C. B. Ruff, *Proc. Natl. Acad. Sci. U.S.A.* **103**, 3552 (2006).
11. Y. Rak, B. Arensburg, *Am. J. Phys. Anthropol.* **73**, 227 (1987).
12. L. Bondioli *et al.*, *J. Hum. Evol.* **50**, 479 (2006).
13. C. O. Lovejoy, *Gait Posture* **21**, 95 (2005).
14. C. Ruff, *Am. J. Phys. Anthropol.* **133**, 698 (2007).
15. R. Potts *et al.*, *Science* **305**, 75 (2004).
16. F. Spoor *et al.*, *Nature* **448**, 688 (2007).
17. G. P. Rightmire, D. Lordkipanidze, A. Vekua, *J. Hum. Evol.* **50**, 115 (2006).
18. D. Lordkipanidze *et al.*, *Nature* **449**, 305 (2007).
19. R. G. Tague, *Am. J. Phys. Anthropol.* **80**, 59 (1989).
20. J. DeSilva, J. Lesnik, *J. Hum. Evol.* **51**, 207 (2006).
21. R. L. Holloway, D. C. Broadfield, M. S. Yuan, *The Human Fossil Record: Brain Endocasts* (Wiley-Liss, Hoboken, NJ, 2004).
22. H. Coqueugniot, J.-J. Hublin, F. Veillon, F. Houët, T. Jacob, *Nature* **431**, 299 (2004).
23. C. Dean *et al.*, *Nature* **414**, 628 (2001).
24. R. G. Tague, *Am. J. Phys. Anthropol.* **127**, 392 (2005).

25. H. Correia, S. Balseiro, M. De Areia, *J. Comp. Hum. Biol.* **56**, 153 (2005).
26. D. Walrath, thesis, University of Pennsylvania, Philadelphia (1997).
27. C. B. Ruff, *Yearb. Phys. Anthropol.* **37**, 65 (1994).
28. The Gona Project thanks the Authority for Research and Conservation of Cultural Heritage of the Ministry of Culture and Tourism, and the National Museum of Ethiopia, for research permits and support. Support for this research was provided by the L. S. B. Leakey Foundation, National Geographic Society, Wenner-Gren Foundation, and NSF. We are grateful for the overall support of K. Shick and N. Toth (co-directors of CRAFT). We appreciate the hospitality of the Afar administration at Semera and our Afar colleagues from Eloha. We thank Y. Haile-Selassie and L. Jellema (Cleveland Museum of Natural History) for allowing us to examine materials in their care. Discussions with and comments by C. O. Lovejoy, R. G. Tague, Y. Haile-Selassie, G. Suwa, T. White, G. WoldeGabriel, B. Latimer, B. Asfaw, S. Standen, R. Byrne, and anonymous reviewers were helpful. A. Admasu's help at the National Museum of Ethiopia is appreciated.

Supporting Online Material
www.sciencemag.org/cgi/content/full/322/5904/1089/DC1
Materials and Methods
SOM Text
Figs. S1 to S11
Tables S1 to S10
References

22 July 2008; accepted 14 October 2008
10.1126/science.1163592

Slide into Action: Dynamic Shuttling of HIV Reverse Transcriptase on Nucleic Acid Substrates

Shixin Liu,[1] Elio A. Abbondanzieri,[1] Jason W. Rausch,[4] Stuart F. J. Le Grice,[4] Xiaowei Zhuang[1,2,3]*

The reverse transcriptase (RT) of human immunodeficiency virus (HIV) catalyzes a series of reactions to convert single-stranded viral RNA into double-stranded DNA for host cell integration. This process requires a variety of enzymatic activities, including DNA polymerization, RNA cleavage, strand transfer, and strand displacement synthesis. We used single-molecule fluorescence resonance energy transfer to probe the interactions between RT and nucleic acid substrates in real time. RT was observed to slide on nucleic acid duplexes, rapidly shuttling between opposite termini of the duplex. Upon reaching the DNA 3′ terminus, RT can spontaneously flip into a polymerization orientation. Sliding kinetics were regulated by cognate nucleotides and anti-HIV drugs, which stabilized and destabilized the polymerization mode, respectively. These long-range translocation activities facilitate multiple stages of the reverse transcription pathway, including normal DNA polymerization and strand displacement synthesis.

Retroviral reverse transcriptase (RT) is a multifunctional enzyme that catalyzes conversion of the single-stranded viral RNA genome into integration-competent double-stranded DNA. RT possesses several distinct activities, including DNA- and RNA-dependent DNA synthesis, DNA-directed RNA cleavage, strand transfer, and strand displacement synthesis, all of which are required to complete the reverse transcription cycle (fig. S1) (*1*, *2*). The enzyme first uses viral RNA as the template to synthesize minus-strand DNA (*3*, *4*), and the resulting DNA/RNA hybrid is then cleaved by the ribonuclease H (RNase H) activity of RT to produce short RNA fragments hybridized to nascent DNA (*5*, *6*). Specific RNA fragments, known as the polypurine tracts (PPTs), serve as primers for synthesis of plus-strand DNA from the minus-strand DNA template (*7*–*9*). Secondary structures present in the viral RNA genome, as well as the nontemplate strands hybridized to the DNA template, require RT to perform strand displacement synthesis during both minus- and plus-strand DNA synthesis (*10*–*16*).

[1]Department of Chemistry and Chemical Biology, Harvard University, Cambridge, MA 02138, USA. [2]Department of Physics, Harvard University, Cambridge, MA 02138, USA. [3]Howard Hughes Medical Institute, Harvard University, Cambridge, MA 02138, USA. [4]HIV Drug Resistance Program, National Cancer Institute, Frederick, MD 21702, USA.

*To whom correspondence should be addressed. E-mail: zhuang@chemistry.harvard.edu

As a major target for anti-HIV therapy, RT has been the subject of extensive research. Crystal structures, biochemical assays, and single-molecule analyses have suggested different modes of interaction between RT and nucleic acid substrates, providing snapshots of the nucleoprotein complexes that illuminate the functional mechanism of RT [e.g., (*17*–*25*)]. Nevertheless, how the enzyme-substrate complex acquires specific functional configurations and switches between different functional modes remains unclear. For example, how does RT efficiently locate the 3′ terminus of nascent DNA on a long duplex substrate to initiate DNA polymerization? This question is particularly important for a low-processivity polymerase such as RT, which must frequently locate the polymerization site after dissociation (*10*, *26*). Perhaps even more puzzling is how the dissociated RT locates the polymerization site during strand displacement synthesis, considering that the primer terminus may itself be displaced from the template by the competing nontemplate strand. Also, RT cleaves at many different sites within a DNA/RNA hybrid, but how it accesses these sites remains incompletely understood (*21*, *22*). A dynamic visualization of RT interacting with different substrates will help us address these questions and gain a more complete understanding of its function.

In this work, we used fluorescence resonance energy transfer (FRET) (*27*, *28*) to monitor in real time the action of individual HIV-1 RT molecules and their interactions with various nucleic acid substrates. We specifically labeled RT with the FRET donor dye Cy3 at either the RNase H domain (H-labeled) or the fingers domain (F-labeled) of its catalytically active p66 subunit (fig. S2A) (*2*, *29*, *30*). A $Glu^{478}\rightarrow Gln^{478}$ (E478Q) mutation was introduced to eliminate RNase H activity (*31*) and prevent degradation of the nucleic acid substrates during experiments. Nucleic acid substrates were labeled with the FRET acceptor dye Cy5 at various sites, specifically immobilized on a quartz surface, and immersed in a solution containing Cy3-labeled RT (fig. S2B) (*2*). Fluorescence from individual RT-substrate complexes was monitored with a total-internal-reflection fluorescence (TIRF) microscope by using an alternating laser excitation scheme (*32*). The observed FRET value allowed the binding configuration of the enzyme to be determined (fig. S2C) (*2*). Control experiments showed that neither dye labeling nor surface immobilization notably affected the enzyme activity (fig. S3) and that photophysical properties of the FRET dyes did not change appreciably when placed in proximity to the enzyme (fig. S4) (*2*).

To mimic substrates encountered by RT during minus-strand synthesis, we constructed a series of hybrid structures of various lengths, each consisting of a DNA primer and an RNA template with Cy5 attached to one of two sites: (i) near the 3′ end of the RNA template, which we define as the back end of the hybrid ("back-labeled," Fig. 1, A to C), or (ii) near the 5′ end of the RNA template and 3′ end of the DNA primer, which we define as the front end ("front-labeled," fig. S5, B and C) (*2*). On a 19–base pair (bp) hybrid, a length chosen to approximate its footprint on nucleic acid duplexes (*17*, *33*), RT bound in only one configuration: Binding of H-labeled RT to the back-labeled substrate yielded uniformly high FRET values (centered at 0.95) (Fig. 1A), indicating that RT bound with its RNase H domain close to the back end of the hybrid. Considering that the RNase H and polymerase active sites are at opposite ends of the substrate binding cleft of RT, this configuration places the polymerase active site of the RT over the 3′ terminus of the DNA primer, consistent with the polymerization-competent binding mode observed in crystal structures (*17*, *18*).

In contrast, two distinct binding modes were observed on longer DNA/RNA hybrids. H-labeled RT bound to back-labeled 38-bp hybrid yielded two FRET peaks centered at 0.95 and 0.39, re-

spectively (Fig. 1B). The FRET value of 0.39 is quantitatively consistent with RT binding in polymerization competent mode, in which the polymerase active site is located over the primer terminus at the front end of the hybrid, placing the Cy3 dye ~19 bp away from the Cy5 label. The high-FRET peak at 0.95 indicates an additional binding mode in which the RNase H domain is located near the back end of the hybrid, which apparently cannot support polymerase activity. The equilibrium constant between the front- and back-end binding states was 3.3:1. Moving the biotin from the 5′ end of the DNA primer (i.e., near the back end of the hybrid) to the 5′ end of the RNA template (i.e., near the front end) resulted in a nearly identical equilibrium constant (3.1:1), again suggesting a minimal effect of surface immobilization. These two binding modes at the front and back end of the hybrid were further confirmed by two additional FRET labeling schemes in which F-labeled or H-labeled RT was added to the front-labeled substrate (fig. S5) (*2*). The two end-binding states also predict further separation of the two FRET peaks as the length of the hybridized region increases, which was experimentally confirmed with a 56-bp hybrid. Binding of H-labeled RT to the back-labeled 56-bp hybrid produced two FRET peaks centered at 0 and 0.95, also with a ~3:1 partition ratio (Fig. 1C).

Taken together, these results indicate that the enzyme can stably bind either to the front end of the hybrid poised for DNA extension or to the back end, placing the RNase H domain close to the 3′ end of the RNA template. The front-end binding state of RT should also support RNase H activity. The two binding modes were independent of hybrid sequence and the nature of the hybrid termini, that is, whether they feature recessed

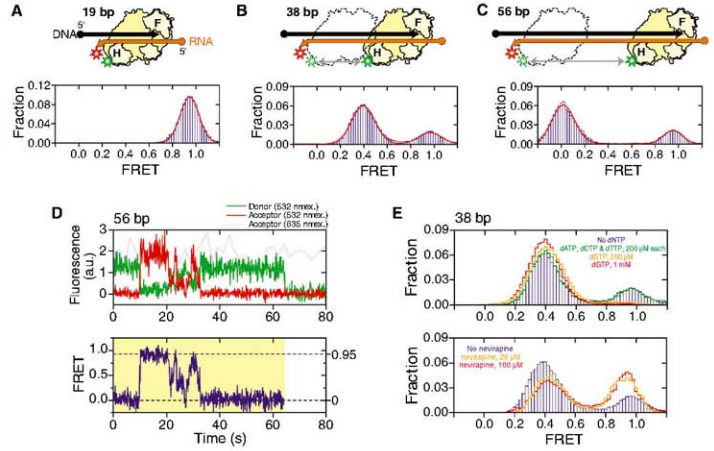

Fig. 1. RT slides on nucleic acid substrates. (**A** to **C**) H-labeled RT (yellow) bound to a 19-bp (A), 38-bp (B), and 56-bp (C) back-labeled DNA (black)/RNA (orange) hybrid. F and H on the enzyme represent the fingers and RNase H domains, respectively. Circle and arrow on the nucleic acid strands represent 5′ and 3′ ends, respectively. Green and red stars indicate Cy3 and Cy5 dyes, respectively. The FRET histograms (blue) were fit with a single (A) or double [(B) and (C)] Gaussian peaks (red line). (**D**) Representative fluorescence (top) and FRET (bottom) time traces of RT bound to a 56-bp DNA/RNA hybrid at 12°C, showing gradual transitions between the 0 and 0.95 FRET states and the preferred intermediates near FRET ~ 0.3 to 0.5. The time resolution is 10 Hz. The green and red traces represent donor and acceptor fluorescence under 532-nm excitation, and the pink trace represents acceptor fluorescence under 635-nm excitation. The yellow shade marks a single RT binding event. a.u., arbitrary units. (**E**) Effects of nucleotides and nevirapine on sliding. (Top) FRET histograms of RT bound to the 38-bp DNA/RNA hybrid in the absence of nucleotides (blue), in the presence of the cognate dGTP (orange and red), or noncognate nucleotides (green). The DNA primer was chain-terminated to prevent elongation. (Bottom) FRET histograms in the absence (blue) and presence of nevirapine (orange and red).

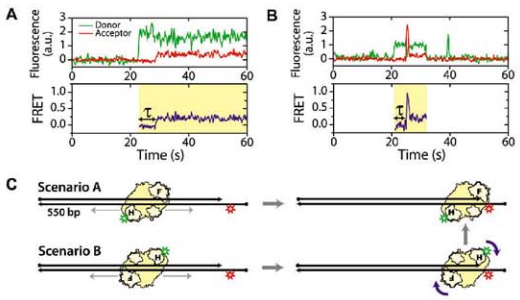

Fig. 2. Sliding of RT facilitates polymerization site targeting. H-labeled RT was added to a ~550-bp DNA duplex with Cy5 attached near the front end. Binding of RT to the polymerization site at the duplex front end is expected to give a FRET value of 0.3. (**A**) Donor and acceptor fluorescence and corresponding FRET time traces of a typical binding event show a time delay (τ) between binding of RT and placing of RT at the polymerization site. (**B**) A binding event showing a transient 0.9 FRET state between the 0 and 0.3 FRET states, suggesting that RT arrived at the front end in an orientation that placed the RNase H domain close to the primer terminus and subsequently flipped to the polymerization orientation. The time resolution of the traces is 10 Hz. Cy5 fluorescence under direct 635-nm excitation (omitted for clarity) indicates that an active Cy5 is present during the whole detection time. Yellow shades in the FRET time traces mark individual RT binding events. The histogram of the time delay, τ, is shown in fig. S9. (**C**) Schematic depiction of the two primer terminus search scenarios as suggested by traces in (A) and (B).

DNA or RNA (fig. S6) (*2*). They were also independent of whether the RNase H-inactivating E478Q mutation was introduced (fig. S5) (*2*). To further test whether sliding was a general activity of RT, we exchanged the RNA template in the DNA/RNA hybrid for a DNA template to emulate plus-strand DNA synthesis. RT was again observed to slide between the termini of the duplex DNA, although the transition rates between the two ends were different from those observed on the DNA/RNA hybrid (fig. S7) (*2*).

The FRET time traces of individual RT molecules showed repeated transitions between the front- and back-end bound states within a single binding event (Fig. 1D), suggesting shuttling between the two ends of the hybrid without dissociation. The FRET transitions between the two end states were not instantaneous but rather gradual, with preferred intermediate states in the middle of the hybrid (Fig. 1D and fig. S8, A and B) (*2*). Shuttling motion sped up as the temperature was raised (fig. S8C) but did not require nucleotide hydrolysis, suggesting that the movement is a thermally driven diffusion process. RT was previously observed to cleave RNA at multiple positions within a DNA/RNA hybrid (*5*, *21*, *22*) in a manner consistent with the end-binding states and the sliding intermediates observed here, suggesting that sliding may provide a mechanism for RT to rapidly access these cleavage sites.

It is remarkable that a polymerase could frequently slide away from the polymerization site. To explore what structural rearrangements within the enzyme may be required for this action, we tested the effects of small molecule ligands on sliding kinetics. Binding of a cognate nucleotide is expected to cause the fingers and thumb domains of RT to form a tighter grip around the primer terminus (*34*) and stabilize the polymerization state. To test the effect of nucleotide binding, we again used H-labeled RT and back-labeled 38-bp DNA/RNA hybrid but with 3′-dideoxyribonucleoside-terminated DNA primer to prevent DNA synthesis. Addition of 2′-deoxyguanosine 5′-triphosphate (dGTP), the next cognate nucleotide, significantly stabilized the low FRET front-end bound state (Fig. 1E), further supporting the notion that the front-end bound state reflects RT binding in the polymerization-competent mode. Kinetically, addition of 1 mM dGTP slowed down the rate constant of front to back transitions ($k_{front \rightarrow back}$) by 12-fold without substantially affecting the reverse rate constant $k_{back \rightarrow front}$ (fig. S7C) (*2*). In contrast, addition of mismatched nucleotides [2′-deoxyadenosine 5′-triphosphate (dATP), 2′-deoxycytidine 5′-triphosphate (dCTP), and 2′-deoxythymidine 5′-triphosphate (dTTP)] did not significantly affect the transition kinetics (Fig. 1E). Another small molecule ligand tested was the nonnucleoside RT inhibitor (NNRTI), one of the major classes of anti-HIV drugs that inhibit DNA synthesis (*30*, *35*). We measured the sliding dynamics of RT in the presence of nevirapine, a representative NNRTI. Interestingly, the effects of the drug were opposite to those of the cognate deoxyribonucleotide triphosphate (dNTP): Addition of nevirapine destabilized the front-end bound state of the enzyme (Fig. 1E) by increasing $k_{front \rightarrow back}$ without significantly altering $k_{back \rightarrow front}$ (fig. S8C) (*2*). Structurally, NNRTI and cognate dNTP have opposite effects on the conformation of RT near the polymerase active site (*34*, *35*): Whereas nucleotide binding tightens the clamp of the fingers and thumb domains around the substrate, binding of NNRTI loosens

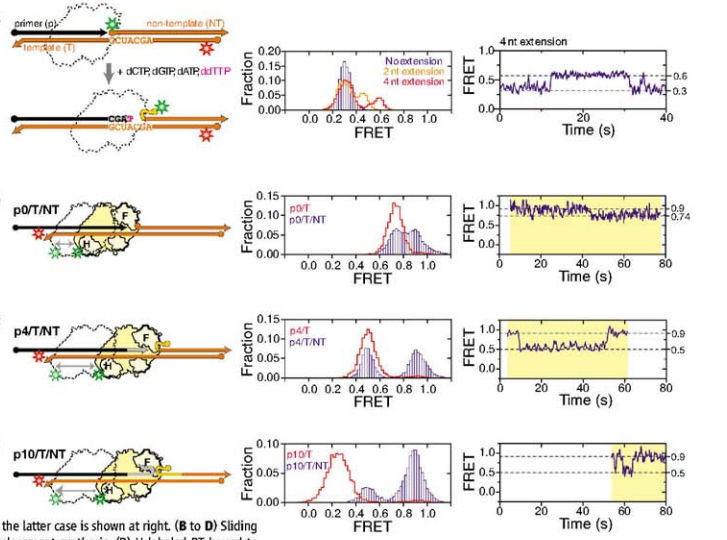

Fig. 3. RNA strand displacement synthesis. **(A)** Substrate structural dynamics during strand displacement synthesis. RT and nucleotides were added to Cy3/Cy5 doubly labeled p0/T/NT substrate to initiate synthesis. Overlapping sequence within the p and NT strands are colored in light gray and light orange, respectively. The corresponding FRET histograms are shown in the middle. Blue bars represent the FRET distribution in the presence of RT but absence of nucleotides. The orange line indicates the distribution in the presence of dCTP, ddGTP, dATP, and dTTP; and the red line indicates the distribution in the presence of dCTP, dGTP, dATP, and ddTTP, allowing a two- and a four-nucleotide extension, respectively. A representative FRET time trace for the latter case is shown at right. **(B** to **D)** Sliding of RT during RNA strand displacement synthesis. (B) H-labeled RT bound to back-labeled p0/T/NT. The corresponding FRET histogram (middle, blue) and representative time trace (right) show dynamic transitions between two FRET states (0.74 and 0.9). Overlaid on the FRET histogram is the FRET distribution of RT bound to the p0/T substrate lacking the NT strand (red line). (C and D) As above except that p0/T/NT is replaced by p4/T/NT (C) or p10/T/NT (D) to mimic the extended substrates encountered during RNA displacement synthesis. The corresponding FRET histograms (middle, blue bars) and time traces (right) show dynamic transitions between FRET states of 0.5 and 0.9. Overlaid in red lines are the FRET distributions of RT bound to the corresponding pX/T duplex without the NT strand. Yellow shades in the right graphs mark individual RT binding events, all of which started with FRET = 0.9, indicating initial binding to the back end of the pX/T region. Time resolutions of the traces are 10 Hz in (A), (B), and (D) and 5 Hz in (C). All measurements were done in the presence of dNTPs, and the primer 3′ terminus was chain-terminated to prevent elongation.

the clamp. Hence, our data suggest that relaxation of the fingers-thumb grip is likely required for RT to escape the polymerization site. Our observation that NNRTI promotes enzyme escape from the polymerization site also suggests an inhibitory mechanism for this class of drugs and explains why the inhibitory effect of NNRTI is stronger on long DNA synthesis than on short DNA synthesis (*36*).

Next, we probed potential functional roles of RT sliding on reverse transcription. Compared to cellular DNA polymerases, RT exhibits poor processivity, typically dissociating from the substrate after synthesizing only a few to a few hundred nucleotides (*10*, *26*), despite a ~10-kb-long HIV genome (*37*). RT thus frequently encounters the challenge of having to locate the nascent DNA terminus to continue DNA synthesis. The ability of RT to slide on duplexes suggests an interesting mechanism of enzyme targeting by one-dimensional search, a mechanism that has been proposed for target searching by transcription factors, RNA polymerase, and DNA repair enzyme (*38*–*42*). To test this possibility, we added H-labeled RT to a ~550-bp front-labeled DNA duplex (Fig. 2). Were RT to bind directly to the duplex front end, we would expect a FRET value of 0.3 immediately upon binding, corresponding to the ~19-bp distance expected between Cy3 and Cy5. Instead, we found that the majority of the binding events initiated with a FRET value of 0, reaching 0.3 only after a finite time delay (Fig. 2A and fig. S9). This observation indicates that the enzyme first bound to the DNA outside the polymerization site and subsequently moved to the primer terminus where polymerization takes place (Fig. 2C). Such a binding procedure will likely increase the polymerization target searching efficiency on long duplexes where the primer terminus constitutes only a tiny fraction of the duplex substrate. However, if the enzyme can indeed bind in the middle of a duplex, the lack of directional cues may also lead to binding in the "wrong" orientation, such that the RNase H domain is poised closer than the polymerase domain to the 3′ terminus of the primer (Fig. 2C). In this case, even after sliding to the front end, RT would not be properly positioned for DNA synthesis. This type of binding was indeed observed frequently (~48% of the time), as indicated by a high FRET state with FRET ~0.9, after the initial 0 FRET state (Fig. 2B). Remarkably, the high FRET state converted rapidly into the 0.3 FRET state in situ without dissociation (Fig. 2B), indicating that the enzyme flipped into the polymerization-competent orientation. The ability of RT to flip to the polymerization orientation once reaching the primer terminus without dissociation may further increase its target searching efficiency. Our data does not exclude a possibility that the enzyme may also flip in the middle of the duplex, although such flipping events should not lead to a net increase of target searching efficiency.

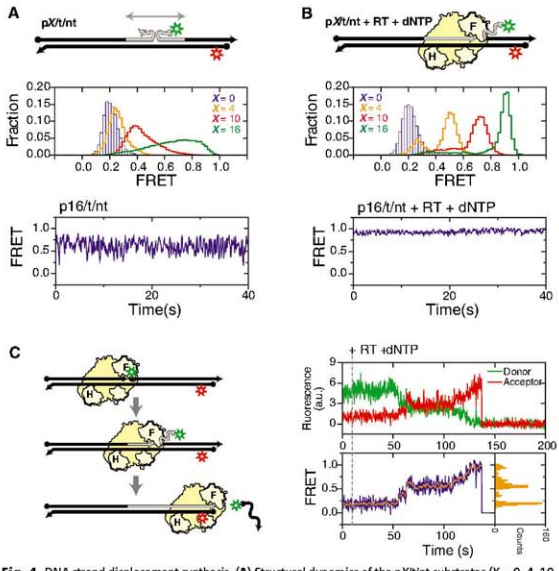

Fig. 4. DNA strand displacement synthesis. **(A)** Structural dynamics of the p*X*/t/nt substrates (*X* = 0, 4, 10, and 16) consisting of all DNA strands. The corresponding FRET histograms are shown in the middle and a representative FRET time trace (*X* = 16) in the bottom. **(B)** As in (A) but in the presence of RT and dNTPs. The primers were terminated with a dideoxyribonucleoside to prevent elongation. **(C)** Single-molecule detection of DNA displacement synthesis. RT and dNTPs were added to the p0/t/nt substrate to initiate DNA synthesis in situ. FRET gradually increased as reaction progressed because of the unzipping of the nontemplate strand. Completion of the reaction was marked by the abrupt loss of the fluorescence signal because of dissociation of the donor labeled nontemplate strand. Plateaus were observed in the donor/acceptor fluorescence traces (top) and the FRET trace (blue trace in bottom left graph), indicating pausing events during synthesis. As a corollary, distinct peaks were observed in the histogram (bottom right inset) constructed from the FRET trace smoothed by 9-point average (orange trace in bottom left graph). Time resolutions are 16 Hz in (A) and (B) and 10 Hz in (C).

Hairpins and long duplexes present on the template strand during DNA synthesis require the polymerization machinery to perform strand displacement synthesis. Polymerization site targeting on these substrates may be even more challenging because, after enzyme dissociation, these template secondary structures could displace the nascent primer terminus to occlude the polymerization site. This is especially problematic in the case of intrastrand RNA displacement during minus-strand synthesis because duplex RNA is more stable than a DNA/RNA hybrid (*43*, *44*). To probe the structural dynamics of substrates encountered during RNA strand displacement synthesis, we designed a series of FRET-labeled triple-stranded substrates, each consisting of an RNA template (T) to which a complementary DNA primer (p) and RNA nontemplate strand (NT) were simultaneously hybridized, with the Cy3 and Cy5 dyes flanking the T/NT duplex region (Fig. 3A). We use the notation p*X*/T/NT to represent a substrate whose primer has been extended by *X* nucleotides. As expected, the FRET distributions for substrates with all *X* values displayed a peak at 0.3, identical to that observed for the nonextended p0/T/NT substrate (fig. S10), indicating that the T/NT duplex was fully annealed and that the extended DNA primers were not able to displace the NT RNA.

We then added RT and dNTPs to the p0/T/NT substrate to monitor substrate dynamics during displacement synthesis. In the absence of dNTP, a single FRET peak centered at 0.3 was again observed (Fig. 3A). After addition of dNTPs to initiate primer extension and selected dideoxyribonucleotide triphosphate (ddNTP) to terminate synthesis at specific positions, FRET was observed to increase because of unwinding of the T/NT duplex. The presence of dCTP, ddGTP, dATP, and dTTP supported a two-nucleotide addition, producing a higher FRET peak at 0.45 (Fig. 3A). This higher FRET peak further increased

to 0.6 in the presence of dCTP, dGTP, dATP, and ddTTP, which allowed a four-nucleotide extension (Fig. 3A). The FRET distribution agreed quantitatively with that observed for the preassembled, chain-terminated p4/T/NT substrate in the presence of RT and dNTPs (fig. S11) (*2*), confirming successful primer extension. FRET time traces of individual molecules showed repetitive transitions between the 0.6 and 0.3 FRET states (Fig. 3A), suggesting frequent reannealing of the T and NT strands.

One possible cause for T/NT reannealing is sliding of RT to the back end of the p/T hybrid, leaving its front end unbound. To test this experimentally, we added Cy3-labeled RT and dNTPs to Cy5-labeled p*X*/T/NT substrates, the primers of which were chain-terminated to prevent extension (Fig. 3, B to D). Indeed, transitions between a high and a relatively low FRET state were observed. The high FRET state (0.9) indicates proximity of RT to the back end of the p/T hybrid. The lower FRET states (0.74 for p0/T/NT and 0.5 for p4/T/NT) quantitatively agree with those observed for the p0/T and p4/T hybrids lacking the NT strand (Fig. 3, B and C), to which RT should predominantly bind at the front end in the presence of dNTPs. These results indicate that RT shuttles between the polymerization site and the back end of the substrate even during displacement synthesis.

In the absence of enzyme, a stable T/NT RNA duplex was formed (fig. S10) and no spontaneous annealing of the p*X*/T hybrid was observed in the FRET time traces. The low processivity of RT poses another question: How would the enzyme, after dissociation, locate the polymerization site (i.e., the front end of the primer/template hybrid) again if such a structure is rarely formed? The answer can be found in the FRET traces: The vast majority (~90%) of the binding events on the p*X*/T/NT substrates started at the back end with high FRET, with RT subsequently sliding forward to assume the front-end binding state with relatively low FRET (Fig. 3C, right). These observations suggest that sliding allows the enzyme to kinetically access the disrupted polymerization site and assist primer-template annealing, thereby facilitating RNA strand displacement synthesis.

Interestingly, on a substrate with a longer primer extension (p10/T/NT), FRET was also observed to switch between the same 0.9 and 0.5 states as observed for the p4/T/NT substrate (Fig. 3D). Had the primer/template hybrid fully annealed, binding of RT to the front end of the hybridized region would yield FRET values significantly lower than 0.5, as observed for the p10/T substrates lacking the NT strand (Fig. 3D). Similar results were found for the p5/T/NT substrate. These data indicate that RT was not able to slide all the way to the front end of the primer once the overlap between the p and NT strands exceeded four nucleotides. Moreover, the enzyme predominantly remained at the back end of the substrate. We thus expect the efficiency of strand displacement synthesis to drop accordingly. This was directly confirmed by an ensemble primer extension assay, which revealed that primer extension primarily terminated after adding five nucleotides through RNA strand displacement synthesis (fig. S12A) (*2*). The exact termination sites were sequence-dependent, consistent with previous observations (*16*).

The energetic difference between the p*X*/T and T/NT duplexes observed during RNA strand displacement synthesis does not exist in DNA strand displacement synthesis because all strands involved in the latter case are DNA. To examine substrate dynamics during DNA strand displacement synthesis, we doubly labeled all DNA primer/template/nontemplate substrates (defined as p*X*/t/nt) with Cy3 and Cy5 (Fig. 4A). In contrast to the p*X*/T/NT counterparts, the FRET distributions were substantially broader for nonzero primer extension (X = 4, 10, and 16), and rapid FRET fluctuations were observed in single-molecule traces (Fig. 4A). These observations suggest frequent exchanges between the primer and nontemplate strands for base-pairing with the template. After addition of RT and dNTPs to the substrates (chain-terminated to prevent primer extension), the FRET distribution predominantly assumed a high FRET value that consistently increased with X (Fig. 4B), suggesting that RT reached the front end of the p/t duplex and unwound the t/nt duplex. Even in the case of DNA displacement synthesis, the primer was rarely fully annealed to the template in the absence of a bound RT. It is likely that RT is also targeted to the polymerization site by first binding to the intact part of the primer/template duplex and subsequently sliding forward to unwind the nontemplate strand and anneal the primer. Because there is no substantial energy penalty for exchanging DNA base pairs, RT was thus able to access the primer terminus regardless of the length of the primer extension (Fig. 4B), consistent with RT's ability to perform displacement synthesis through long DNA duplexes (*12*). When RT and dNTPs were added to the nonterminated p0/t/nt substrate to support synthesis, an increase in FRET was observed as the nt strand was displaced (Fig. 4C). Once the FRET donor-labeled nt strand was fully displaced, a sudden drop in the total fluorescence signal reflected completion of the reaction (Fig. 4C). Rapid and complete DNA strand displacement synthesis was observed for nearly all molecules (fig. S12) (*2*). Frequent pausing was also observed during synthesis, indicated by plateaus in the single-molecule FRET trace (Fig. 4C). The origin of these kinetic pausing events and their relation to the preferred synthesis termination sites (*23*, *45*) will be a subject of future investigation.

HIV-1 RT thus appears to be a highly dynamic enzyme that can spontaneously slide over long distances on DNA/RNA and DNA/DNA duplex structures, which facilitates multiple phases of reverse transcription, including targeting RT to the primer terminus for DNA polymerization, allowing the enzyme to rapidly access multiple sites within an RNA/DNA hybrid during viral RNA degradation, as well as displacing the nontemplate strand and annealing the primer terminus during displacement synthesis. The dynamic flexibility further extends into orientational conformations, allowing the enzyme to flip between opposite binding orientations that support different activities (*21*, *25*). Flipping and sliding can be combined in a complex series of enzyme movements to enhance its efficacy: RT molecules originally bound in the opposite orientation were observed to spontaneously flip into the polymerization orientation after sliding to the primer terminus. It is remarkable that an enzyme could have such large-scale orientational and translational dynamics. This type of dynamic flexibility may be a general design principle for multifunctional enzymes like HIV RT, helping them to rapidly access different binding configurations required to accomplish different functions.

References and Notes

1. A. Telesnitsky, S. P. Goff, in *Retroviruses*, J. M. Coffin, S. H. Hughes, H. E. Varmus, Eds. (Cold Spring Harbor Laboratory Press, Cold Spring Harbor, NY, 1997), pp. 121–160.
2. Materials and methods are available as supporting material on *Science* Online.
3. D. Baltimore, *Nature* **226**, 1209 (1970).
4. H. M. Temin, S. Mizutani, *Nature* **226**, 1211 (1970).
5. J. P. Leis, I. Berkower, J. Hurwitz, *Proc. Natl. Acad. Sci. U.S.A.* **70**, 466 (1973).
6. J. Hansen, T. Schulze, W. Mellert, K. Moelling, *EMBO J.* **7**, 239 (1988).
7. J. K. Smith, A. Cywinski, J. M. Taylor, *J. Virol.* **49**, 200 (1984).
8. C. A. Omer, R. Resnick, A. J. Faras, *J. Virol.* **50**, 465 (1984).
9. W. I. Finston, J. J. Champoux, *J. Virol.* **51**, 26 (1984).
10. H. E. Huber, J. M. McCoy, J. S. Seehra, C. C. Richardson, *J. Biol. Chem.* **264**, 4669 (1989).
11. M. Hottiger, V. N. Podust, R. L. Thimmig, C. McHenry, U. Hubscher, *J. Biol. Chem.* **269**, 986 (1994).
12. S. H. Whiting, J. J. Champoux, *J. Virol.* **68**, 4747 (1994).
13. G. M. Fuentes, P. J. Fay, R. A. Bambara, *Nucleic Acids Res.* **24**, 1719 (1996).
14. Z. Suo, K. A. Johnson, *Biochemistry* **36**, 12459 (1997).
15. C. D. Kelleher, J. J. Champoux, *J. Biol. Chem.* **273**, 9976 (1998).
16. C. Lanciault, J. J. Champoux, *J. Biol. Chem.* **279**, 32252 (2004).
17. A. Jacobo-Molina *et al.*, *Proc. Natl. Acad. Sci. U.S.A.* **90**, 6320 (1993).
18. S. G. Sarafianos *et al.*, *EMBO J.* **20**, 1449 (2001).
19. S. G. Sarafianos *et al.*, *EMBO J.* **21**, 6614 (2002).
20. W. Metzger, T. Hermann, O. Schatz, S. F. Le Grice, H. Heumann, *Proc. Natl. Acad. Sci. U.S.A.* **90**, 5909 (1993).
21. J. J. DeStefano, L. M. Mallaber, P. J. Fay, R. A. Bambara, *Nucleic Acids Res.* **21**, 4330 (1993).
22. M. Wisniewski, M. Balakrishnan, C. Palaniappan, P. J. Fay, R. A. Bambara, *J. Biol. Chem.* **275**, 37664 (2000).
23. J. Winshell, B. A. Paulson, B. D. Buelow, J. J. Champoux, *J. Biol. Chem.* **279**, 52924 (2004).
24. P. J. Rothwell *et al.*, *Proc. Natl. Acad. Sci. U.S.A.* **100**, 1655 (2003).
25. E. A. Abbondanzieri *et al.*, *Nature* **453**, 184 (2008).
26. K. J. Williams, L. A. Loeb, M. Fry, *J. Biol. Chem.* **265**, 18682 (1990).
27. L. Stryer, R. P. Haugland, *Proc. Natl. Acad. Sci. U.S.A.* **58**, 719 (1967).
28. T. Ha *et al.*, *Proc. Natl. Acad. Sci. U.S.A.* **93**, 6264 (1996).
29. Z. Hostomsky, Z. Hostomska, T. B. Fu, J. Taylor, *J. Virol.* **66**, 3179 (1992).
30. L. A. Kohlstaedt, J. Wang, J. M. Friedman, P. A. Rice, T. A. Steitz, *Science* **256**, 1783 (1992).
31. J. W. Rausch, B. K. Sathyanarayana, M. K. Bona, S. F. Le Grice, *J. Biol. Chem.* **275**, 16015 (2000).